Draft version October 9, 2019
Typeset using LaTeX **preprint2** style in AASTeX62

Four (Super)Luminous Supernovae From the First Months of the ZTF Survey

R. Lunnan,[1] Lin Yan,[2] D. A. Perley,[3] S. Schulze,[4] K. Taggart,[3] A. Gal-Yam,[4] C. Fremling,[5] M. T. Soumagnac,[4,6] E. Ofek,[4] S. M. Adams,[5] C. Barbarino,[1] E. C. Bellm,[7] K. De,[5] C. Fransson,[1] S. Frederick,[8] V. Z. Golkhou,[7,9] M. J. Graham,[5] N. Hallakoun,[10] A. Y. Q. Ho,[5] M. M. Kasliwal,[5] S. Kaspi,[10] S. R. Kulkarni,[5] R. R. Laher,[11] F. J. Masci,[11] F. Pozo Nuñez,[12,13] B. Rusholme,[11] R. M. Quimby,[14] D. L. Shupe,[11] J. Sollerman,[1] F. Taddia,[1] J. van Roestel,[5] Y. Yang,[4] and Yuhan Yao[5]

[1] *The Oskar Klein Centre & Department of Astronomy, Stockholm University, AlbaNova, SE-106 91 Stockholm, Sweden*

[2] *Caltech Optical Observatories, California Institute of Technology, Pasadena CA 91125, USA*

[3] *Astrophysics Research Institute, Liverpool John Moores University, 146 Brownlow Hill, Liverpool L3 5RF, UK*

[4] *Department of Particle Physics and Astrophysics, Weizmann Institute of Science, Rehovot 76100, Israel*

[5] *Division of Physics, Mathematics and Astronomy, California Institute of Technology, Pasadena, CA 91125, USA*

[6] *Lawrence Berkeley National Laboratory, 1 Cyclotron Road, Berkeley, CA 94720, USA*

[7] *DIRAC Institute, Department of Astronomy, University of Washington, 3910 15th Avenue NE, Seattle, WA 98195, USA*

[8] *Department of Astronomy, University of Maryland, College Park, MD 20742, USA*

[9] *The eScience Institute, University of Washington, Seattle, WA 98195, USA*

[10] *School of Physics and Astronomy, Tel-Aviv University, Tel-Aviv 6997801, Israel*

[11] *IPAC, California Institute of Technology, 1200 E. California Blvd, Pasadena, CA 91125, USA*

[12] *Haifa Research Center for Theoretical Physics and Astrophysics, University of Haifa, Haifa, Israel*

[13] *Astronomisches Institut, Ruhr–Universität Bochum, Universitätsstraße 150, 44801 Bochum, Germany*

[14] *Department of Astronomy/Mount Laguna Observatory, San Diego State University, 5500 Campanile Drive, San Diego, CA 92812-1221, USA*

Submitted to ApJ

ABSTRACT

We present photometry and spectroscopy of four hydrogen-poor luminous supernovae discovered during the two-month science commissioning and early operations of the Zwicky Transient Facility (ZTF) survey. Three of these objects, SN 2018bym (ZTF18aapgrxo), SN 2018avk (ZTF18aaisyyp) and SN 2018bgv (ZTF18aavrmcg) resemble typical SLSN-I spectroscopically, while SN 2018don (ZTF18aajqcue) may be an object similar to SN 2007bi experiencing considerable host galaxy reddening, or an intrinsically long-lived, luminous and red SN Ic. We analyze the light curves, spectra, and host galaxy properties of these four objects and put them in context of the population of SLSN-I. SN 2018bgv stands out as the fastest-rising SLSN-I observed to date, with a rest-frame g-band rise time of just 10 days from explosion to peak – if it is powered by

Corresponding author: Ragnhild Lunnan
ragnhild.lunnan@astro.su.se

magnetar spin-down, the implied ejecta mass is only $\simeq 1$ M$_\odot$. SN 2018don also displays unusual properties – in addition to its red colors and comparatively massive host galaxy, the light curve undergoes some of the strongest light curve undulations post-peak seen in a SLSN-I, which we speculate may be due to interaction with circumstellar material. We discuss the promises and challenges of finding SLSNe in large-scale surveys like ZTF given the observed diversity in the population.

Keywords: supernovae:general , supernovae:individual (SN2018avk, SN2018don, SN2018bym, SN2018bgv) — surveys

1. INTRODUCTION

In the past decade, wide-field transient surveys have greatly expanded the parameter space of known stellar explosions. One such intriguing new type of supernova is the "superluminous" supernovae (SLSNe), initially broadly defined as supernovae with peak absolute magnitudes < -21 mag (Gal-Yam 2012; see Gal-Yam 2019 for a recent review). Now with more than 100 such objects reported (e.g., Guillochon et al. 2017; Gal-Yam 2019), the observed diversity of the class is growing but trends are emerging. It has been shown that most SLSNe without hydrogen in their spectra (SLSN-I) form a distinct spectroscopic class, and can be separated from other stripped-envelope supernovae based on their spectra alone (Quimby et al. 2018); the observed luminosity function of SLSN-I selected spectroscopically does extend fainter than -21 mag (Lunnan et al. 2018a; De Cia et al. 2018; Angus et al. 2019). For SLSNe with hydrogen in their spectra (SLSN-II), most display intermediate-width Balmer lines, classifying them spectroscopically as SN IIn. There are also examples of SLSN-II with broad Balmer lines, however (Gezari et al. 2009; Miller et al. 2009; Inserra et al. 2018b), as well as objects classified as SLSN-I based on their peak spectra that show signatures of interaction with H-rich material at late times (Yan et al. 2015, 2017), complicating the picture.

One reason why SLSNe have garnered so much attention in the community is that the underlying physical mechanism behind their enormous luminosities is still not well-understood. One class of models, particularly for the SLSN-I, involves energy injection from the spin-down of a millisecond magnetar born in the explosion (Kasen & Bildsten 2010; Woosley 2010). This model has proved successful in explaining the light curves and spectra of a wide variety of SLSN-I (Inserra et al. 2013; Liu et al. 2017a; Nicholl et al. 2018a; Dessart et al. 2012; Dessart 2019), including out to very late times (Nicholl et al. 2018b). Direct evidence of a central engine, such as the predicted X-ray breakout at late times (Metzger et al. 2014) has largely remained elusive, however (Margutti et al. 2018; Bhirombhakdi et al. 2018); one exception may be the recent detection of radio emission from the position of the SLSN-I PTF10hgi consistent with a young magnetar nebula (Eftekhari et al. 2019). Alternative explanations include circumstellar interaction, in which large amounts of kinetic energy can be converted to radiation as the ejecta collides with and shocks a dense circumstellar medium (CSM) (Chevalier & Irwin 2011; Chatzopoulos et al. 2012; Moriya et al. 2013; Sorokina et al. 2016; Wheeler et al. 2017). This model is certainly relevant to the SLSN-II that show narrow emission lines indicating CSM interaction; while such spectroscopic signatures are not seen in SLSN-I, observations such as light curve undulations (e.g. Nicholl et al. 2016; Vreeswijk et al. 2017; Blanchard et al. 2018b), late-time Hα emission (Yan et al. 2015, 2017)

and the recent direct detection of a CSM shell around a SLSN-I through a light echo (Lunnan et al. 2018b) at least shows that some SLSN-I progenitors experience significant mass loss close to explosion. Finally, some SLSN-I have been proposed to be powered by radioactive decay of ^{56}Ni through the pair-instability explosion of a very massive star (helium core mass $M_{\rm He} \approx 65 - 130 M_\odot$; Barkat et al. 1967; Heger & Woosley 2002; Woosley et al. 2007). The large ejecta masses and therefore long implied diffusion times means this model is only applicable to the slowest-evolving SLSNe, however, and even for these objects it is debated (Gal-Yam et al. 2009; Nicholl et al. 2013; Lunnan et al. 2016; Jerkstrand et al. 2016; Gomez et al. 2019).

The SLSN discovery rate has accelerated in the past decade, much thanks to untargeted transients surveys like the Panoramic Survey Telescope and Rapid Response System (Pan-STARRS; Chambers et al. 2016), the Palomar Transient Factory (PTF; Rau et al. 2009), the Asteroid Terrestrial-impact Last Alert System (ATLAS; Tonry et al. 2018b), the *Gaia* Photometric Science Alerts programme[1] (Gaia Collaboration et al. 2016), and the All-Sky Automated Survey for Supernovae (ASAS-SN; Shappee et al. 2014). The Zwicky Transient Facility (ZTF), with an upgrade to a 47 square degree camera (compared to 7.8 square degrees in its predecessor PTF) represents a new generation of transient surveys, and functions as an important intermediate step between PTF-scale surveys and the upcoming Large Synoptic Survey Telescope (LSST) in the 2020s.

Here, we present the discovery, data, and analysis of the first SLSN-I from ZTF, discovered during the commissioning and science validation period (April-May 2018). The total number of SLSN-I found during this period was four; we focus our analysis on two particularly noteworthy events: SN 2018bgv (ZTF18aavrmcg), which shows unusually rapid timescales for a SLSN-I; and SN 2018don (ZTF18aajqcue), a heavily reddened event that shows unusual light curve variation post-peak. This paper is structured as follows. Section 2 details the discoveries, ZTF photometry and follow-up data. We analyze the supernova properties and place them in context of the population of SLSNe in Sections 3 and 4, and do the same with their host galaxies in Section 5. We discuss our results in the context of diversity within the population of (super)luminous supernovae, and prospects and implications for studying SLSNe with large surveys such as ZTF in Section 6, and summarize our findings in Section 7. Throughout this paper, we assume a flat ΛCDM cosmology with $\Omega_{\rm M} = 0.27$, $\Omega_\Lambda = 0.73$, and $H_0 = 70$ km s^{-1} Mpc^{-1} (Komatsu et al. 2011).

2. DATA

2.1. *ZTF Survey Overview*

The Zwicky Transient Facility (Bellm et al. 2019a; Graham et al. 2019) is an optical time-domain survey utilizing a new, 47 square degree field of view camera (Dekany et al. 2016) on the Palomar 48-inch telescope. A public-private partnership, the time is divided between public surveys (40%), surveys undertaken by the ZTF partnership (40%), and Caltech surveys (20%); an overview of the major surveys undertaken in Year 1 is given in Bellm et al. (2019b). The data is processed real-time at IPAC (Masci et al. 2019), including a novel image differencing algorithm (Zackay et al. 2016) and machine learning based vetting of candidates (Mahabal et al. 2019; Duev et al. 2019). Transient candidates are then distributed in alert packages using the Apache Avro format[2]

[1] http://gsaweb.ast.cam.ac.uk/alerts/

[2] https://avro.apache.org/

and distributed using the Apache Kafka streaming system[3] (Patterson et al. 2019).

The objects described in this paper were identified following alert filtering using the GROWTH marshal (Kasliwal et al. 2019), first in a general "science validation" filter requiring multiple detections, positive subtractions, not coincident with a point source (using star-galaxy scores derived by Tachibana & Miller (2018) based on PS1 images) , and not rejected as an artifact by the machine learning (though this threshold was set low, as the model was still being trained at this stage). Thus, these transients were not initially flagged as SLSN candidates, but rather identified as such as more photometry, spectroscopic follow-up or external information became available. Our goal here is not to present a carefully selected or complete sample, but rather to showcase the variety of luminous supernovae found in a short time period by ZTF, and discuss implications for SLSN selection strategies in large surveys. We focus our attention on the two most unusual objects, SN 2018bgv and SN 2018don, which could have indeed easily been missed by stricter filtering on "typical" SLSN properties such as long rise times, blue colors and/or faint host galaxies. The full first two year sample of ZTF SLSNe will be presented by Perley et al. (2019, in preparation) and Yan et al. (2019, in preparation).

2.2. *SLSNe found in early ZTF data*

In this section we list the details of the discovery and classification of the four SNe discussed in this paper. The coordinates, redshifts and Galactic extinction for each object are listed in Table 1. These objects were all detected by multiple surveys; we describe the survey first reporting the transient to the Transient Name Server[4] (TNS) as the "discovery" regardless of when the first ZTF detection was. Since all the objects discussed here are from the beginning of the survey, the ZTF template images contain varying amounts of transient flux in most cases. Thus, the first ZTF alert issued is typically later than the first ZTF detection of the transient, as recovered in reprocessing the images.

2.2.1. *ZTF18aaisyyp = SN 2018avk*

SN 2018avk was discovered by Gaia (as Gaia18ayq) on 2018 Apr 14 and reported to the TNS on 2018 Apr 16 (Delgado et al. 2018a). The transient is clearly present in the ZTF reference images; running subtractions using a PS1 reference image as described in Section 2.3.1 we find the earliest ZTF detection to be 2018 Mar 25.32 at $g = 20.54 \pm 0.12$ mag. Due to the presence of transient flux in the reference, the first ZTF alert was 2018 Apr 11.26 (as ZTF18aaisyyp). A spectrum taken with the Andalucia Faint Object Spectrograph and Camera (ALFOSC) on the 2.5m Nordic Optical Telescope (NOT) on 2018 May 04 gives a redshift of $z = 0.132$ from narrow host galaxy lines, and features matching typical SN Ic, consistent with the classification reported by Nicholl et al. (2018a). Combined with the light curve information, this indicates SN 2018avk is a SLSN-I, with the first spectra taken slightly after peak.

2.2.2. *ZTF18aapgrxo = SN 2018bym*

SN 2018bym was discovered by ATLAS on 2018 May 10 (as ATLAS18ohj) and reported to the TNS (Tonry et al. 2018a,b); the first ZTF detection (as ZTF18aapgrxo) was 2018 Apr 21.49, at $g = 20.94 \pm 0.14$ mag. An initial spectrum taken with NOT+ALFOSC shows a blue continuum with shallow absorption features, consistent with the O II absorptions typically seen in SLSN-I (Quimby et al. 2011, 2018) at a redshift $z \simeq 0.28$ (assuming an expansion velocity of $10,000$ km s^{-1}). Narrow emission lines in the classification spectrum reported by Blanchard et al. (2018a) gives the host galaxy

[3] https://kafka.apache.org/
[4] https://wis-tns.weizmann.ac.il/

redshift $z = 0.274$, which is also confirmed in our own follow-up spectroscopy.

2.2.3. *ZTF18aavrmcg = SN 2018bgv*

SN 2018bgv was discovered by Gaia (as Gaia18beg) on 2018 May 6 and reported to the TNS on 2018 May 8 (Delgado et al. 2018b). Again the ZTF reference image contains transient flux; running host subtraction with PS1 pre-explosion images we find that ZTF caught the full rise and peak of this transient, with the first detection on 2018 May 5.18 at $r = 19.73 \pm 0.06$ mag. Again due to significant transient flux in the reference image, the first ZTF alert (as ZTF18aavrmcg) was not until 2018 May 22.17, at which point the transient had already been publicly classified as a SLSN-I at $z \simeq 0.08$ by Dong et al. (2018). Narrow emission lines from the host galaxy seen in our subsequent spectra give a precise redshift of $z = 0.0795$.

2.2.4. *ZTF18aajqcue = SN 2018don*

SN 2018don was first detected in ZTF data on 2018 Apr 14.32 as ZTF18aajqcue, though again it is also likely present in the reference images. A spectrum taken with the Double Beam Spectrograph (DBSP; Oke & Gunn 1982) on the 200-in Hale telescope at Palomar Observatory (P200) gives the redshift $z = 0.0734$ from narrow emission and absorption lines, and shows spectroscopic features similar to slowly evolving SLSNe such as SN 2007bi (Gal-Yam et al. 2009) and PS1-14bj (Lunnan et al. 2016). This long-lived transient was also discovered by Pan-STARRS (as PS18aqo) on 2018 Jun 16, and reported to the TNS by them on 2018 Jul 13, given the IAU name 2018don (Chambers et al. 2018).

2.3. *Photometry*

2.3.1. *P48 photometry*

The ZTF photometric pipeline and data products are described in Masci et al. (2019). However, since the supernovae discussed here were discovered at the very beginning of the survey, the objects have varying degrees of supernova flux present in the reference images, meaning the pipeline photometry in the alert packages will report magnitudes that are too faint. Additionally, if an object falls on multiple fields/quadrants each of these will have a separate reference image which may in turn contain different amounts of supernova flux, resulting in considerable scatter in the default photometry – this is the case for SN 2018don (3 fields) and SN 2018avk (2 fields).

For this reason, we reprocess the light curves using the ZTF forced photometry service (Masci et al. 2019), which performs forced PSF-fit photometry on the archived difference images. This allows us to adjust the flux baseline for each field/filter combination using data taken after the supernovae has faded below ZTF detectability (generally, we find this to be the case for the 2019 observing season). This will correct the photometry for any transient flux present in the template, but will not recover any of the epochs from the time period that went into making the template images used. For two objects, SN 2018avk and SN 2018bgv, a significant part of the light curve is contained in the images that went into building the reference. For these, we use FPipe (Fremling et al. 2016) to redo the subtractions using Pan-STARRS1 (PS1; Chambers et al. 2016; Flewelling et al. 2016) images as references. We find that the photometry from the two pipelines agree well up to a small zeropoint offset, and shift the FPipe photometry to be consistent with the IPAC forced photometry. All photometry is reported in Table 2, and the light curves are shown in Figure 1.

2.3.2. *LT photometry*

We acquired multi-filter observations of several of the SLSNe discussed in this work with the optical imager (IO:O) on the robotic Liver-

pool Telescope (LT; Steele et al. 2004) located at the Observatorio del Roque de los Muchachos on La Palma. Observations were taken in the g, r, i, or z bands. We use reduced images provided by the basic IO:O pipeline, stacking using SWarp in cases where multiple exposures were taken on a given night. Digital image subtraction was performed versus PS1 reference imaging, again following the techniques of Fremling et al. (2016). PSF photometry was performed relative to PS1 photometric standards.

2.3.3. *Wise photometry*

In addition, we observed SN 2018bgv in g' and r' band with the 0.71-m C28 Jay Baum Rich and the 1-m telescopes at the Wise Observatory in Israel. The data were reduced in a standard fashion, including bias correction and flat fielding and the calibration of the world-coordinate system, using the Matlab package for astronomy and astrophysics (Ofek 2014).

These data were obtained when the host contamination was minimal. Hence, we applied aperture photometry, using the tool presented in Schulze et al. (2018)[5], to extract the light curve. To measure the zeropoint of each image, we measured the brightness of several stars in the same way and compared their instrumental magnitudes against tabulated measurements in the SDSS DR9. To mitigate colour differences between Wise and ZTF filter system, we shifted the g'-band data by 0.05 mag and the r'-band data by 0.1 mag.

2.3.4. *Swift photometry*

Three of the supernovae, SN 2018bym, SN 2018avk and SN 2018bgv had UV data obtained with the UV/Optical Telescope (UVOT; Roming et al. 2005) aboard the *Neil Gehrels Swift Observatory* (Gehrels et al. 2004). We retrieved the UVOT data from the NASA *Swift* Data Archive[6], and used the standard UVOT data analysis software distributed with `HEASoft` version 6.19[7], along with the standard calibration data to process it.

In each case, we combined individual integrations of a given epoch in each band using the command `uvotimsum`. For SN 2018avk and SN 2018bym, we measured the flux in a 5″ aperture using the tool `uvotsource`. No host galaxy corrections were applied for these two sources, but the UVOT observations were obtained near peak; based on the host galaxy brightnesses (Section 5) we do not expect this data to be significantly affected by host contamination.

For SN 2018bgv, we do see the UVOT fluxes leveling off in the later epochs suggesting host contamination. To correct for this, we use the data taken between June 22 2018 and November 10 2018 to build a host template. We then measure the flux of the transient in a 6″ circular aperture, and quantify the host flux by applying the same aperture to the template images. We then numerically subtract the host flux from the transient flux to recover the transient photometry. All Swift photometry is reported in Table 2.

2.4. *Spectroscopy*

We obtained classification and follow-up spectra using the Double Beam Spectrograph (DBSP; Oke & Gunn 1982) on the 200-in Hale telescope at Palomar Observatory; the Andalucia Faint Object Spectrograph and Camera (ALFOSC) on the 2.5m Nordic Optical Telescope (NOT); the SPectrograph for the Rapid Acquisition of Transients (SPRAT; Piascik et al. 2014) on the 2m Liverpool Telescope (LT); and the Low Resolution Imaging Spectrometer (LRIS; Oke et al. 1995) on the 10m Keck I telescope. Table 3 lists the de-

[5] https://github.com/steveschulze/Photometry

[6] https://heasarc.gsfc.nasa.gov/cgi-bin/W3Browse/swift.pl

[7] https://heasarc.nasa.gov/lheasoft/

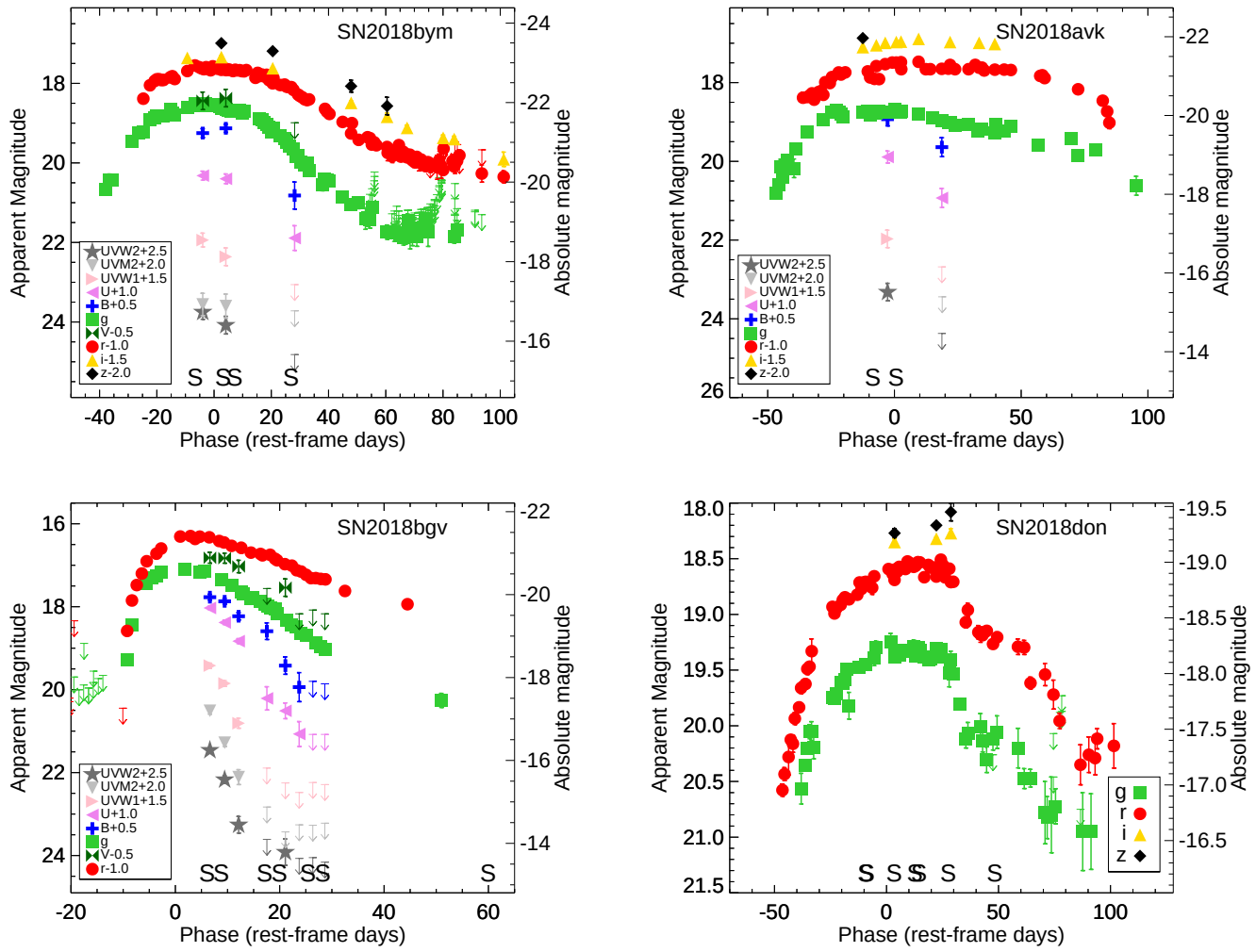

Figure 1. Light curves of the four SLSN-I. Filters are offset as indicated in the individual legends, and the absolute magnitude y-axis on the right side of each plot is calculated assuming a constant K-correction of $2.5 \times \log(1+z)$. Phase is relative to the (rest-frame) g-band peak. ZTF data has been binned by day for presentation purposes. Epochs of spectroscopy are marked with the letter 'S' along the bottom axis.

tails of the spectroscopic observations, and the spectra are displayed in Figures 2 and 3.

Spectra were reduced using standard methods, including wavelength calibration against an arc lamp and using a spectrophotometric standard star for the flux calibration, using available pipelines where possible. For SPRAT spectra we used the automatic reductions supplied in the archive; DBSP spectrum were reduced using a PyRAF-based pipeline (Bellm & Sesar 2016); LRIS spectra were reduced using LPipe (Perley 2019).

2.5. *Host galaxy photometry*

To measure the brightness of the host galaxies from the rest-frame UV to the near-IR, we retrieved science-ready images from the archives of the Galaxy Evolution Explorer Data Release 7 (GALEX; Martin et al. 2005), Panoramic Survey Telescope And Rapid Response System DR1 (PanSTARRS; Flewelling et al. 2016), Sloan Digital Sky Survey DR9 (SDSS; York et al. 2000), Two Micron All-Sky Survey (Skrutskie et al. 2006), and and the unWISE (Lang 2014) images from the NEOWISE Reactivation Year-3

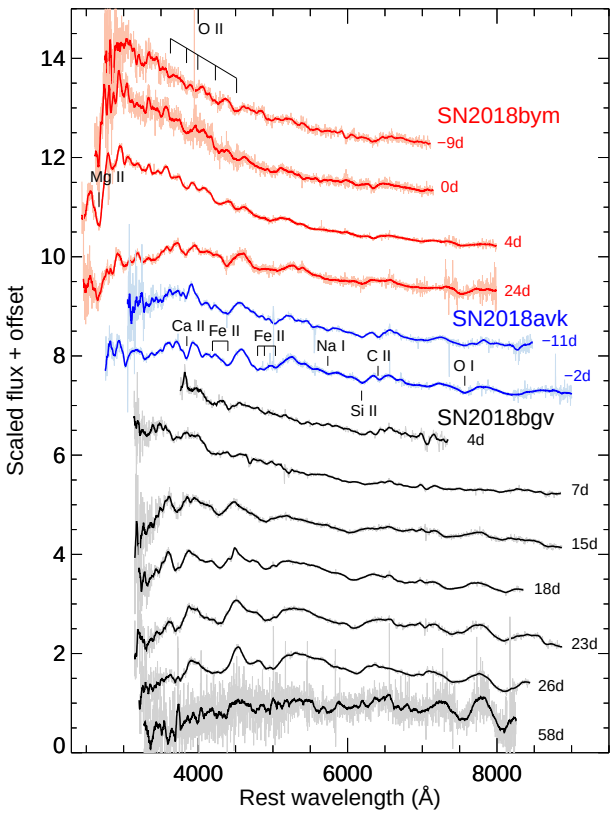

Figure 2. Spectra of three of the SLSN-I: SN 2018bym (red), SN 2018avk (blue) and SN 2018bgv (black). Spectra have been smoothed with a Savitzky-Golay filter; the unsmoothed spectra are shown in the background. Strong host galaxy emission lines have been clipped. As is typical of SLSN-I, pre-peak spectra are dominated by a blue continuum with shallow absorptions, while later-phase spectra resemble those of SN Ic. Some of the strongest typical spectral features are marked.

(Meisner et al. 2017). Furthermore, we augmented the data set of SN 2018bym with deeper optical images from the Canada-France-Hawaii Telescope (CFHT, also science-ready) and complemented the data set of SN 2018bgv with UV data obtained with *Swift*/UVOT. The UVOT images were reduced as described in Section 2.3.4.

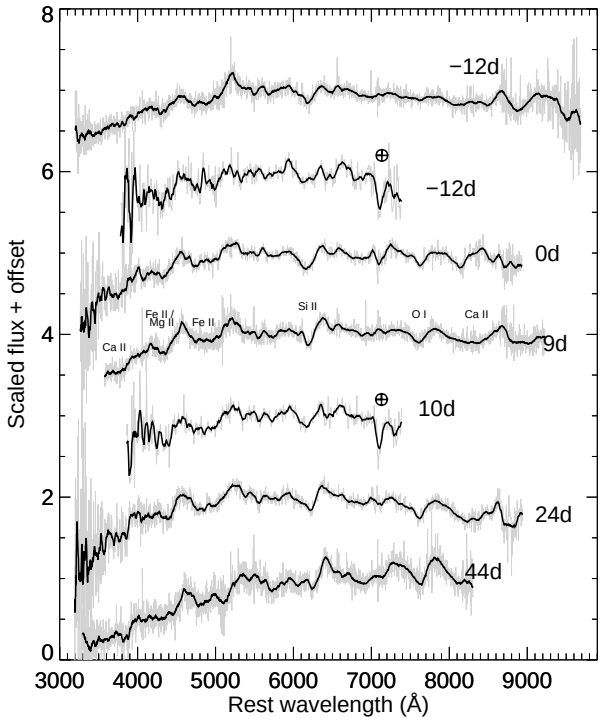

Figure 3. Spectroscopic sequence of SN 2018don. Unsmoothed spectra are shown in gray, while the spectra shown in black have been smoothed with a Savitzky-Golay filter. Areas strongly affected by telluric absorption are marked with a ⊕ symbol, and some of the strongest features are marked on the 9-day spectrum. Unlike the objects shown in Figure 2, SN 2018don shows a significantly redder spectrum and very slow spectroscopic evolution.

We used the software package `LAMBDAR` (Lambda Adaptive Multi-Band Deblending Algorithm in R) (Wright et al. 2016), which is based on a software package written by Bourne et al. (2012), to measure the brightness of each host. `LAMBDAR` has three major input parameters: the point spread function (PSF), the zeropoint and source catalogue (coordinates and parameters of the elliptical apertures) of a given image. With this information in hand, `LAMBDAR` can accurately position an aperture on the pixel grid, modify its shape by the PSF of the to-

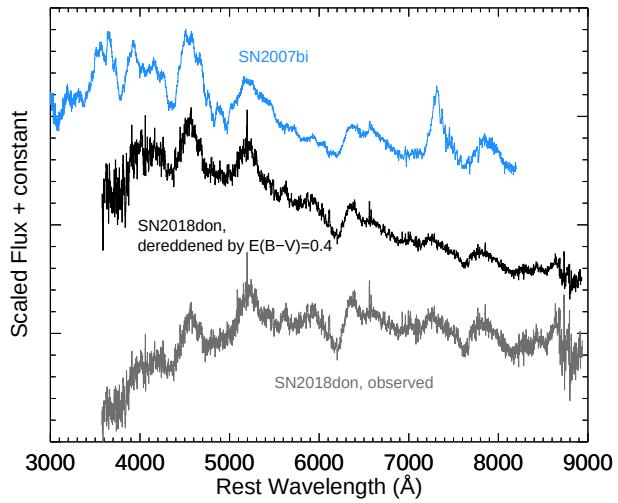

Figure 4. Spectrum of SN 2018don compared to that of SN 2007bi. The bottom (gray) shows a stack of the near-peak SN 2018don spectra, and the middle the same spectrum when dereddened by $E(B-V) = 0.4$ mag and assuming $R_V = 3.1$. This spectrum is a good match to the first spectrum taken of SN 2007bi, shown in blue, with the exception of the strong [Ca II] emission seen from early times in SN 2007bi. Spectra have been arbitrarily scaled and binned for display purposes.

be-analysed image, and accurately measure the brightness while preserving the intrinsic colour.

We used the point-spread functions provided by the *GALEX* in the *GALEX* Technical Documentation[8]. For unWISE images, we used the parameterisation of the PSF from Lang (2014) to generate templates for $W1$ and $W2$. For 2MASS, PS1 and SDSS images, we extracted the median full-width half-maximum of point sources in each image and assumed that the PSFs can be approximated by Gaussian profiles.

We used the tabulated zeropoints for *GALEX*, PanSTARRS, SDSS and unWISE. Specifically, we set the zeropoint of the *GALEX* FUV and NUV images to 18.82 and 20.08 mag(AB) (Morrissey et al. 2007), SDSS images to 22.5 mag(AB)[9], PS1 images to 25+2.5×log(Exposure time) mag(AB)[10], where the exposure time is given in seconds, and unWISE W1 and W2 images to 22.5 mag(Vega) (Lang 2014). To measure the zeropoint of the 2MASS images, we identified several tens of stars in a given field from the 2MASS Point source catalogue and compared the instrumental magnitudes to the tabulated magnitudes. The 2MASS and unWISE zeropoints were converted from the Vega to the AB system using the offsets reported in Cutri et al. (2013) and Blanton & Roweis (2007).

For SN 2018avk, there is a faint galaxy visible $\sim 2.5''$ east of the transient position (~ 6 kpc if at the same redshift). However, there is also diffuse emission at the location of the transient, and strong galaxy emission lines seen in the supernova spectra – given that 6 kpc would be an unusually large offset for a SLSN-I (e.g., Lunnan et al. 2015; Schulze et al. 2018), we assume this diffuse emission is the true host galaxy. We perform photometry at the transient location in the same manner as with the other objects, using an unconvolved aperture radius of $0.75''$.

Table 4 summarizes all host measurements.

3. LIGHT CURVE PROPERTIES

3.1. *Peak luminosities and light curve timescales*

As we do not, in general, have multicolor data available, we do not attempt to construct bolometric light curves for the purposes of measuring light curve properties. Instead, we use the g-band (where available) as our baseline for computing light curve properties such as peak magnitudes and timescales, allowing for easy comparison with the PTF SLSN-I sample published in De Cia et al. (2018). We k-correct the light curves to rest-frame g-band using our available spectra; for light curve points before the earli-

[8] http://www.galex.caltech.edu/wiki/Public:Documentation
[9] https://www.sdss.org/dr12/algorithms/magnitudes/
[10] https://outerspace.stsci.edu/display/PANSTARRS/PS1+FAQ

est spectrum we use the first k-correction measured; for light curves point after the last spectrum we use the last spectrum measured, and for points in between we linearly interpolate between the two closest values. This approach has some drawbacks: as our spectroscopic coverage varies and we will only have a few spectra for some objects, we have to extrapolate the k-correction which introduces uncertainty. On the other hand, the alternative of using some well-measured SLSN (e.g. PTF12dam, as was used by De Cia et al. 2018) will introduce uncertainties due to the potentially different color and spectroscopic evolution of PTF12dam compared to our objects. In practice, since the redshifts of our objects are all $z < 0.3$, the difference between these choices are generally < 0.1 mag.

To measure light curve timescales, we first smooth/interpolate the light curves using Gaussian Process regression. Following Inserra et al. (2018a) and Angus et al. (2019), we use the Python package `george` (Ambikasaran et al. 2015) and an optimized Matern 3/2 kernel to perform the fits. We then measure the peak luminosity in the g-band, and the rise and decline timescales, defined as when the supernova flux is a factor of 2 below peak. The resulting peak times, peak luminosities, and timescales are reported in Table 5.

Figure 5 shows the peak g-band luminosities plotted against rise- and decline timescales, respectively. SN 2018bym and SN 2018bgv both fall within the general cloud of measurements of the De Cia et al. (2018) sample, though SN 2018bgv has a faster rise than any of the objects measured. SN 2018don is both significantly fainter and has a longer rise than most of the PTF objects - if the g-band suffers from $\gtrsim 1.5$ mag extinction, as suggested by spectral comparisons, it would be compatible with the PTF sample luminosity-wise. The steep drop in the light curve of this object affects the measured decline time – had we chosen a different timescale measure (e.g. one magnitude below peak), we would instead have measured a decline timescale of 59 days, closer to that of SN 2018avk. We also note that both SN 2018don and SN 2018avk are examples of relatively faint and long-lived SLSNe, a combination that is rare in the PTF sample.

Since we have coverage of the rising phase of the light curve in g-band for all four objects, we use this to also estimate the explosion dates. We do this by fitting a second-order polynomial to the rise of the observed g-band light curves in flux space, and extrapolating the fit to zero flux. (For SN 2018don, where the observed r-band extends earlier, we use the observed r-band for this calculation instead, though note that we get consistent explosion dates within the error bars using either filter.) The estimated explosion dates for each object are also listed in Table 5. Note that the sharp, well-constrained rise of SN 2018bgv caught in the ZTF data implies that this object had a total rise-time from explosion to peak of only 10 days.

We also note that none of the SLSNe discussed here show evidence of a pre-peak light curve bump, which has been suggested to be an ubiquitous feature of SLSN-I (Nicholl & Smartt 2016; but see also Angus et al. 2019). Our coverage of the earliest phases of the light curves is complicated by the issues with supernova flux in the template images, however; the full ZTF SLSN sample will be able to address this in more detail.

3.2. *Comparison to other SLSNe*

Figure 5 gives some indication of how the SLSN-I discussed here compare to other SLSNe in terms of luminosity and timescale. A more detailed comparison can be done in the phase-space of luminosity, timescale and color, for example using the framework proposed by Inserra et al. (2018a) in their attempt to define SLSN-I statistically. We use our spectra to

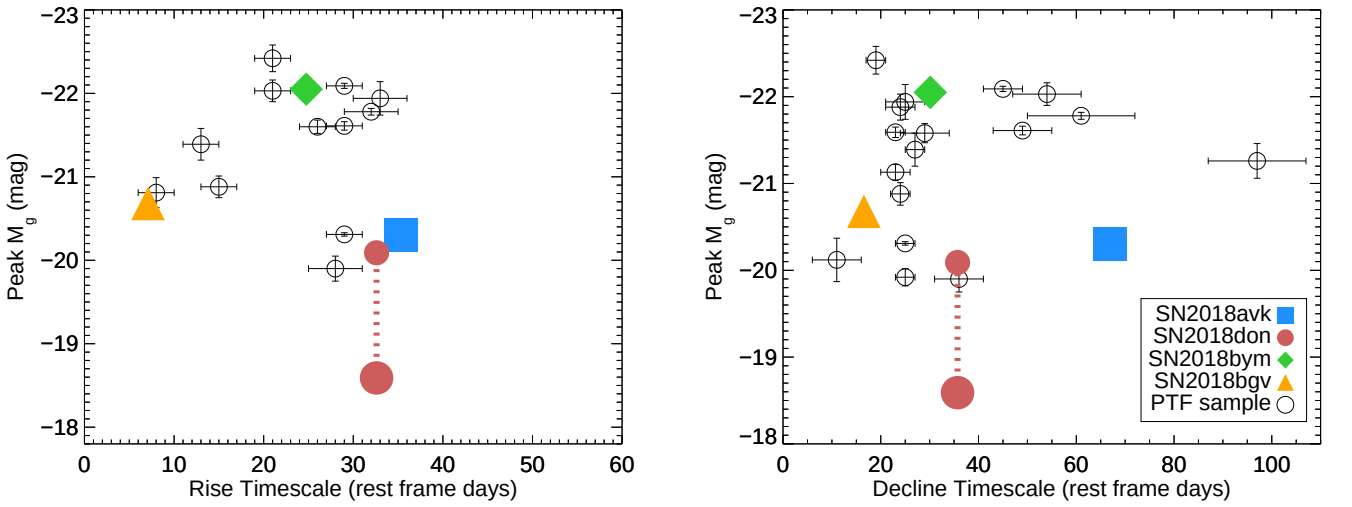

Figure 5. Peak absolute g-band magnitude plotted against rise timescale (left) and decline timescale (right) for the H-poor SNe in our sample. Both timescales are defined as the time between peak and half flux. The smaller circle for SN 2018don shows the peak g-band magnitude if correcting for host galaxy reddening of $E(B-V)=0.4$, corresponding to a 1.5 mag shift in g-band. The PTF sample from De Cia et al. (2018) is shown as circles for comparison.

calculate K-corrections to the fiducial 400 nm and 520 nm bandpasses used in Inserra et al. (2018a), and calculate the peak luminosity and decline rate over 30 days in the 400 nm filter, as well as the $400-520$ color at peak and at 30 days. We find that only SN 2018bym falls within their statistical definition of the "4-observables parameter space"[11]: SN 2018avk is fainter than their sample given its slow decline and relatively blue color 30 days after peak, while SN 2018bgv's color evolution is faster than their sample (i.e., redder than expected 30 days after peak given the very blue color at peak). SN 2018don is, as expected, both fainter and redder than their sample, but this is not surprising if this object is suffering significant host extinction. We note that even when assuming host extinction according to $E(B-V)=0.4$ (which corresponds to 1.8 mag in the 400 nm band and 1.3 mag in the 520 nm band), this object is still too faint and red to be consistent with the "4OPS" parameter space.

Figure 6 shows these same four supernovae compared to some objects with similar light curves in the literature. SN 2018bym has a decay slope similar to SN 2010gx, but its peak luminosity and rise slope more resembles PTF09cnd. The timescales of SN 2018avk are similar to the slowly-evolving PTF12dam, but the peak luminosity is quite a bit fainter, and the overall lightcurve resembles PTF10bjp and PS1-12bqf. For SN 2018bgv, we do not find any clear equivalents in the literature – the decay slope may be similar to fast-evolving objects like PS1-10bzj and SN 2010gx, but the rise is faster and the peak luminosity fainter than either of these. The early light curve appears similar to PTF13bjz, but this object has very sparse data so we cannot ascertain exactly how similar these are.

[11] These four parameters are (1) the peak luminosity in the 400 nm filter, $M(400)_0$; (2) the decline in magnitudes in the 400 nm filter over the 30 days following peak brightness, $\Delta M(400)_{30}$; (3) the $400-520$ color at peak, $M(400)_0 - M(520)_0$; (4) and the $400-520$ color at +30 days, $M(400)_{30} - M(520)_{30}$

SN 2018don, with its steep post-peak drop and subsequent plateau, is shown in comparison to several other literature light curves with pronounced bumps. The most similar in terms of the post-peak slope and second bump is PS1-12cil, but this object had a much faster rise and narrower main peak, so that the rise and decay slope are more consistent. Similarly, iPTF15esb displays a series of bumps, and is similar to SN 2018don on the decline – as the rise was not observed in this object, we cannot ascertain whether its overall light curve would have been more similar to PS1-12cil or SN 2018don. Long-lived SLSNe such as SN 2015bn have also been shown to display post-peak bumps in their light curves, but with less contrast between the bump and an otherwise smooth and slow decline.

3.3. *Color evolution*

An advantage of the Gaussian Process interpolation is that it naturally outputs an estimate of the predicted magnitude and associated uncertainty between data points. We use these g-band magnitudes, together with the interpolated r-band magnitudes, to calculate the $g-r$ colors of our supernovae. The resulting color curves are shown in Fig. 7.

With the exception of SN 2018don, all the supernovae show a color starting out blue and turning redder with time, consistent with an expanding and cooling photosphere. SN 2018bgv stands out in both having the bluest initial colors, and in having the fastest color evolution by far. SN 2018don is significantly redder than the remaining objects throughout its entire evolution. As previously noted, this object could be experiencing significant host galaxy reddening.

We also note that the color of SN 2018don changes during the rapid decline and rebrightening, in particular that the decline in g-band is larger than in r-band. We discuss possible interpretations of this light curve feature and associated color change in Section 6.1.2.

3.4. *Blackbody fits*

We use the code `PhotoFit` (Soumagnac et al. 2019) to fit blackbody functions to epochs where we have at least three filters available (typically, epochs of either *Swift*/UVOT or LT observations). As described in the appendix of Soumagnac et al. (2019), PhotoFit first interpolates the light curve in each filter onto the given epoch, then fits a Planck function at each epoch after correcting for extinction, redshift and filter transmission curves. Both of these fits are performed using Monte Carlo Markov Chain simulations using `emcee` (Foreman-Mackey et al. 2013), allowing for uncertainties to be calculated at each epoch.

The resulting best-fit blackbody temperatures and radii are shown in Figure 8. SN 2018bym and SN 2018bgv show the hottest color temperatures, which is consistent with these two objects also displaying spectra with features corresponding to higher temperatures, such as O II, over this time period. As with the color and overall light curve evolution, SN 2018bgv shows the fastest temperature evolution. The two different values plotted for each epoch of SN 2018don correspond to the results when including the potential host galaxy reddening of $E(B-V) = 0.4$ mag versus not.

4. SPECTROSCOPIC PROPERTIES

4.1. *Spectral Features and Comparisons*

The spectra of SN 2018bym, SN 2018bgv and SN 2018avk all show features that are typical of SLSN-I (e.g., Quimby et al. 2018). In particular, our earliest spectra of both SN 2018bym and SN 2018bgv show blue continua with the characteristic O II "W" - feature around 4500 Å, the strongest of a series of features due to this ion, marked on the top spectrum in Fig. 2. As the ejecta expand and cool, the spectra transition to showing features resembling SNe Ic, with features from Ca II, Fe II, O I, Si II and C I, among others.

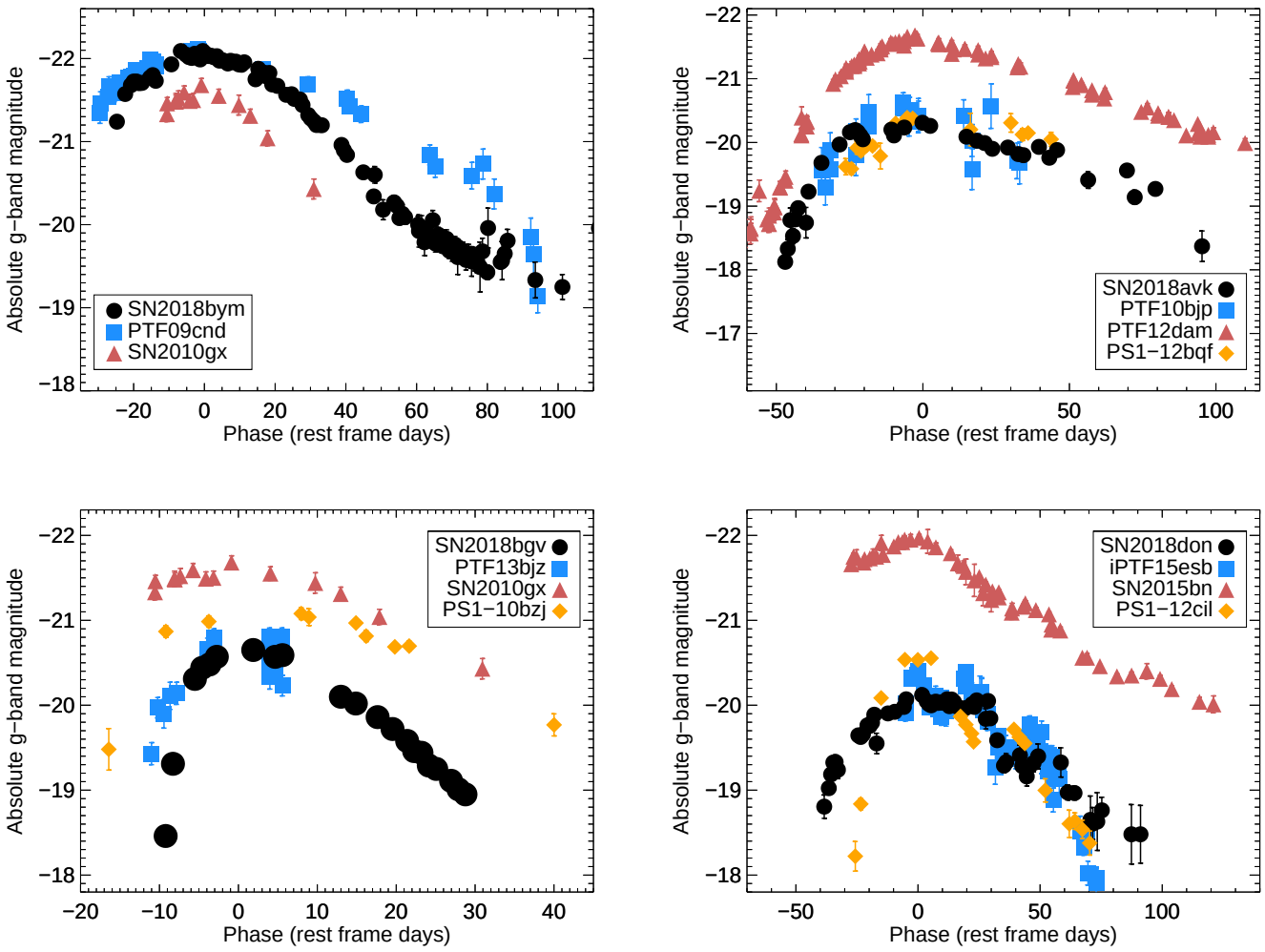

Figure 6. Light curves of the four SLSNe compared to some similar SLSNe from the literature. Comparison data from De Cia et al. (2018), Lunnan et al. (2013, 2018a), Nicholl et al. (2016) and Yan et al. (2017). ZTF data has been binned by day for presentation purposes. K-corrected data is used where available; in the case of slightly higher-redshift objects (PS1-12bqf, PS1-10bzj and PS1-12cil) the observed filter closest to rest-frame g-band is plotted with an approximate K-correction of $2.5 \times \log(1+z)$. The light curve of SN 2018don has been shifted upwards by 1.5 mag, as based on our estimate of the extinction from comparing the spectrum to SN 2007bi (Figure 4).

The spectrum of SN 2018don is significantly redder than the other objects, and shows features generally consistent with a Type I SN – while spectral comparison codes like SNID (Blondin & Tonry 2007) and Superfit (Howell et al. 2005) finds matches to both SNe Ia and Ic, the light curve rules out a SN Ia interpretation. Fig. 4 shows a comparison of the near-peak spectrum of SN 2018don compared to the first spectrum of SN 2007bi (Gal-Yam et al. 2009). The spectral features match well, but the continuum of SN 2007bi is significantly bluer – the spectrum of SN 2018don is a good match if dereddened by E(B-V) = 0.4 mag. If so, the implied extinction in g- and r band is A_g=1.52 mag and A_r=1.09 mag, respectively, again assuming R_V=3.1. This suggests the peak luminosity of SN 2018don was at least −20 mag in r-band, and supports the interpretation of this object as a slowly-evolving SLSN-I.

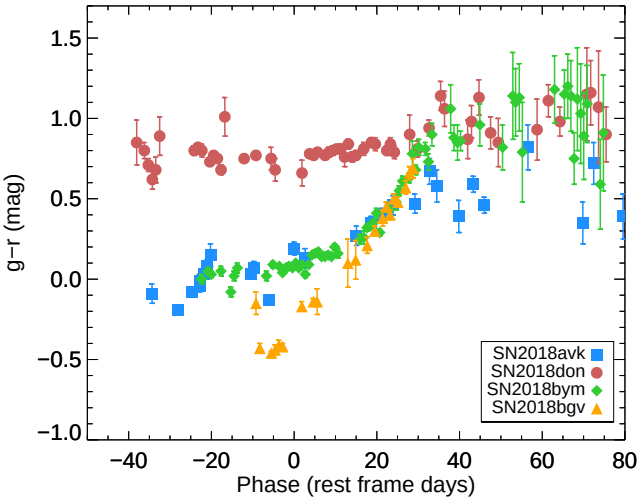

Figure 7. Observed ZTF $g-r$ color of the four supernovae. Color is calculated at the time of the g-band observations (binned by day), and using Gaussian Process interpolation to get the r-band magnitude and uncertainties at the corresponding times. Two objects stand out: SN 2018don, which shows a nearly constant color evolution and is much redder than the other objects; and SN 2018bgv which evolves much faster than the other supernovae.

Compared to the objects shown in Figure 2, the spectroscopic evolution of SN 2018don is slow, with the main features changing little over the nearly 60 days we observe it. The primary features are again typical of SN Ic, and are marked on the +9d spectrum in Figure 3. We do see a clear reddening of the continuum especially in the +44d spectrum – this is partially due to the supernova itself turning redder as the g-band drops faster than the r-band at the light curve break around 30 days, and partially because the host galaxy continuum is starting to contribute significantly to the spectrum at these late epochs. Such a slow spectroscopic evolution has been seen in other SLSN-I of this subtype, for example the well-studied PS1-14bj (Lunnan et al. 2016), which also showed a spectrum similar to SN 2007bi and which hardly showed any evolution over the $\sim$ 60 days of spectroscopic observations in the photospheric phase.

4.2. *Velocities*

Velocities in stripped-envelope supernovae are commonly measured from the absorption minimum of the Fe IIλ5169 feature, which has been suggested to be a good tracer of the photospheric velocity (Branch et al. 2002). We use this feature to measure the velocity of the H-poor SLSNe in our sample, following the method developed in Modjaz et al. (2016) for SNe Ic-BL. This method takes a SN Ic template and applies a blueshift and broadening to match the Fe IIλ5169 and Fe II$\lambda\lambda$4924,5018 features, which are often blended together in both Ic-BL and SLSN-I (Modjaz et al. 2016; Liu et al. 2017b). A complication with applying this technique to SLSNe is that it is not necessarily obvious which phase SN Ic template one should use, since SLSN-I past peak often resemble SN Ic around or before peak (e.g., Pastorello et al. 2010). In principle the template convolution method should be insensitive to which template is used (using a lower-velocity template would result in a larger blueshift measured but the same total velocity), though we find that in spectra of limited S/N there is still some scatter. Therefore, we try a range of template phases for each spectrum, and report the median velocity measured as our best estimate. Typically the template-to-template scatter is smaller than the uncertainties of each velocity measurement; in the cases where it is not we report the standard deviation from the measurements with different templates as the uncertainty.

The velocities we measure are plotted in Figure 9, together with the SLSN-I sample measured by Liu et al. (2017b) using the same method. They caution that in pre-peak measurements, there can be some contamination from Fe III around the wavelength of Fe IIλ5169 in SLSN-I, and only consider measurements 10 days past peak as reliable.

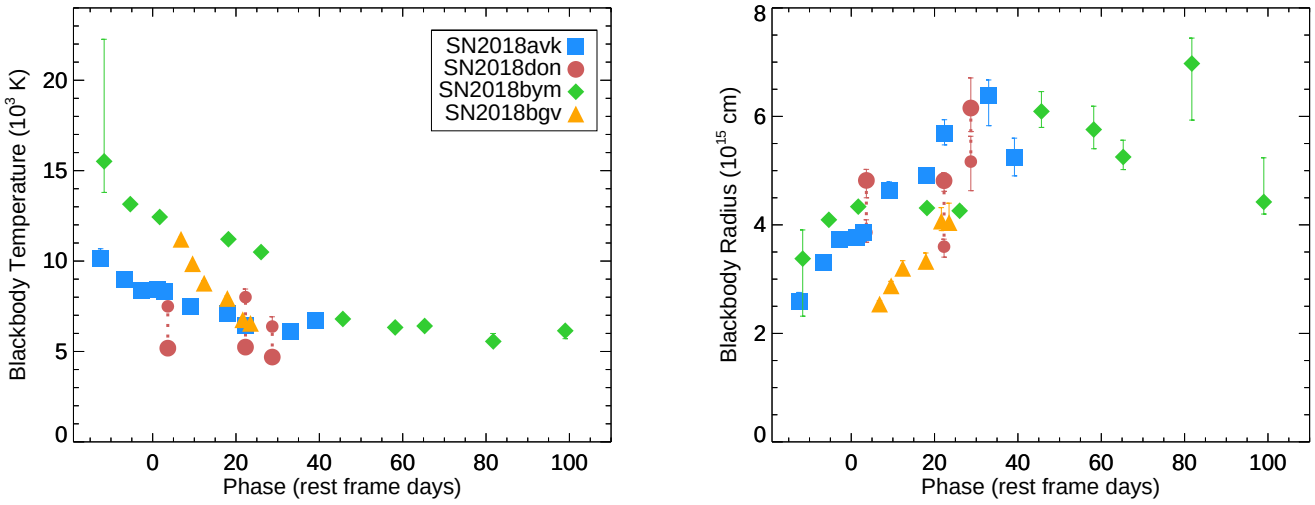

Figure 8. Derived blackbody temperatures (left) and radii (right) from fitting a Planck function to photometry epochs with at least three filters available. The smaller points for SN 2018don show the inferred values if assuming host galaxy extinction according to $E(B-V) = 0.4$ mag.

An alternative to using the Fe II lines at early times is to use the O II lines instead. Figure 9 also shows (as open symbols) the velocities inferred from the O II lines in the first spectra of SN 2018bym and SN 2018bgv, using the wavelengths given in Quimby et al. (2018) as the reference. The velocities from O II are generally lower than those measured from Fe II for these two supernovae, despite being at an earlier phase. This is consistent with the trend found in Quimby et al. (2018) of the O II lines both tracing lower velocities and declining more rapidly than the Fe II lines, indicating that the O II lines form in deeper levels of the ejecta.

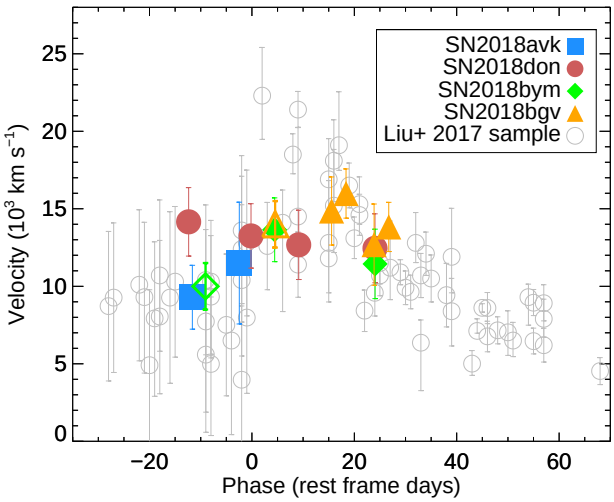

Figure 9. Velocities as measured from the Fe II feature, using the method developed by Modjaz et al. (2016). Data for other SLSNe, taken from Liu et al. (2017b), are shown as gray circles in the background. Also shown, as an open diamond and triangle, respectively, are O II measurements from the earliest spectra of SN 2018bym and SN 2018bgv.

5. HOST GALAXY PROPERTIES

Previous studies have shown that SLSN-I tend to preferentially happen in low-mass, metal-poor dwarf galaxies (Lunnan et al. 2014, 2015; Leloudas et al. 2015; Perley et al. 2016; Angus et al. 2016; Chen et al. 2017a; Schulze et al. 2018). In this section, we fit spectral energy distributions (SEDs) to our compiled archive photometry of the host galaxies (Section 2.5) in order to derive basic host properties and compare to the literature sample.

To fit SEDs, we use the stellar population synthesis code FAST (Kriek et al. 2009), using the Maraston (2005) stellar population library,

a Salpeter initial mass function (IMF), an exponentially declining star formation history and a Milky Way-like extinction curve. While we do not have host galaxy spectra available, several of our supernova spectra do show host emission lines, which we use to inform the model grid metallicities and extinction ranges. In particular, the host of SN 2018avk has strong emission lines, where the ratio of Hα to Hβ constrains the extinction to be close to zero. Similarly, for the SN 2018bym, SN 2018avk and SN 2018bgv host galaxies, we assume a model metallicity of 0.5 $Z_\odot$, while for the host of SN 2018don we assume solar metallicity based on the relatively strong [N II]$\lambda\lambda$6548,6584Å host emission lines compared to Hα seen in the spectra.

The derived host galaxy stellar masses, extinction, stellar population ages and star formation rates are listed in Table 6, and the SED fits are shown in Figure 10. The SEDs of the hosts of SN 2018avk and especially SN 2018bym are not particularly well constrained, and the latter lacks any UV data to constrain the star formation rate in the fit. The host of SN 2018don has the best sampled SED, and is the only galaxy out of the four with derived stellar mass $> 10^9$ $M_\odot$. We note that while the best-fit model (with a reduced χ^2 statistic of 0.6) has $A_V = 0$, models with A_V up to 1.8 are within the 1σ uncertainty range. If we assume $A_V \simeq 1.2$ as suggested by the supernova spectral comparisons, the resulting host model has a similar mass but younger stellar population age (as expected from the age-extinction degeneracy), and the fit has a reduced χ^2 of 1.06. The galaxy photometry is therefore consistent with the possibility that the supernova is significantly reddened.

To put the host galaxies in context, we plot the galaxy stellar masses in Figure 11, compared to literature data over the same redshift range (Perley et al. 2016; Schulze et al. 2018; Bose et al. 2018). The hosts of SN 2018avk, SN 2018bym and SN 2018bgv are consistent with the bulk of SLSN host galaxies at this redshift, which are dominated by dwarf galaxies. The host of SN 2018don stands out by being one of the most massive SLSN-I host galaxies found to date at low redshift – it is not unique, however: the host of PTF10uhf has a derived stellar mass $> 10^{11}$ $M_\odot$ (Perley et al. 2016), and the host of SN 2017egm similarly has a stellar mass of several times 10^{10} $M_\odot$ (Bose et al. 2018; Nicholl et al. 2017a). Thus, SN 2018don adds to the small but growing sample of SLSN-I that occur in high-mass, solar metallicity galaxies. We caution, however, that the global properties of the host galaxy do not necessarily correspond to the conditions at the explosion site, as the study of the very nearby SN 2017egm has shown (Chen et al. 2017b; Izzo et al. 2018; Yan et al. 2018).

6. DISCUSSION

6.1. *Diversity within the SLSN population*

While this paper only presents a few objects, the first SLSNe discovered by ZTF hints at the large diversity present in this population. It is worth noting that out of the four objects discussed here, only SN 2018bym meets the "original" definition of a SLSN (peak absolute magnitude brighter than −21 mag; Gal-Yam 2012) as well as the definition more recently proposed by Inserra et al. (2018a). This is consistent with results from recent compilation studies from untargeted surveys, however: the SLSN samples from Pan-STARRS1 (Lunnan et al. 2018a), (i)PTF (De Cia et al. 2018) and DES (Angus et al. 2019) all find a significant population of objects with spectra consistent with SLSNe but luminosities extending at least down to −20 mag (and in the case of DES, down towards −19 mag).

Additionally, the vast majority of SLSN-I discovered to date display rise timescales significantly slower than the 10 days observed in

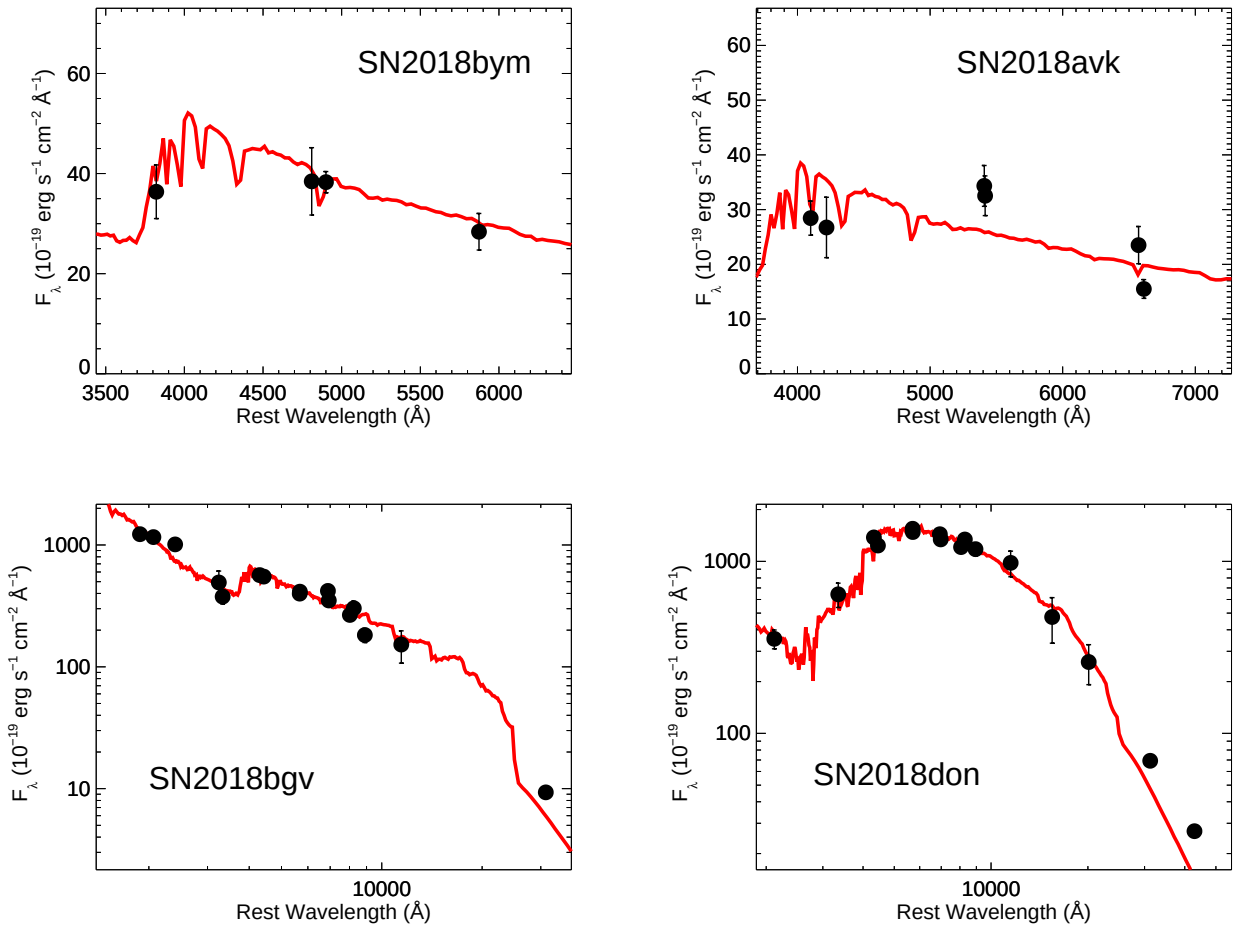

Figure 10. Best-fit host galaxy SEDs, derived with the FAST stellar population synthesis code. Black points show the observed photometry, while the red lines show the model SED. SN 2018bgv and SN 2018don (bottom panels), which have a wider range of data, are shown on a log scale for clarity.

SN 2018bgv (Lunnan et al. 2018a; De Cia et al. 2018). It is not clear whether this reflects the true underlying distribution of timescales in the population, or whether shorter timescale events are underrepresented because an easy way to discriminate most known SLSNe from more common transients like SN Ia is to filter on longer light curve rise times. Complete spectroscopic surveys, such as the ZTF Bright Transient Survey (Fremling et al. 2018; Kulkarni et al. 2018), will play an important role in mapping out the true diversity.

6.1.1. *Powering the Fast Light Curve of SN 2018bgv*

With a rest-frame g-band rise time of just 10 days as measured from the inferred explosion date (and 7 days as measured from time of half peak flux), SN 2018bgv is starting to approach the timescales of so-called "rapidly evolving transients" or "fast, blue, luminous transients" (Drout et al. 2014; Arcavi et al. 2016; Pursiainen et al. 2018; Rest et al. 2018). There does not exist a unified definition of such objects, but is generally applied to transients with luminosities comparable to normal supernovae but significantly faster timescales, ruling out a ^{56}Ni powering mechanism. We note that SN 2018bgv would have met the criteria of Arcavi et al. (2016), who looked at objects

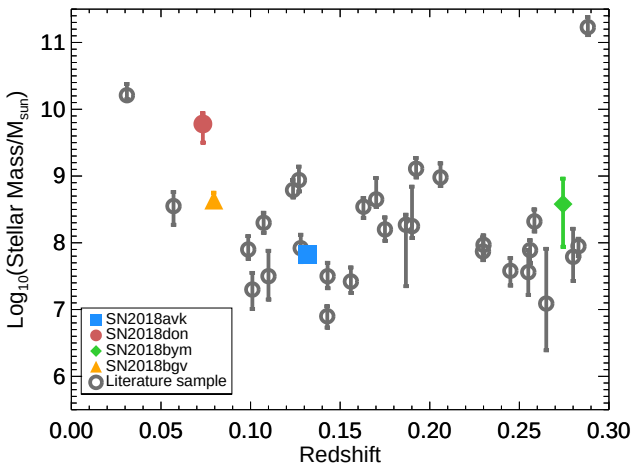

Figure 11. Host galaxy stellar mass plotted as a function of redshift for the four SLSN-I. Literature data for other low-redshift SLSN-I host galaxies are plotted as gray circles.

from the Supernova Legacy Survey with a rise time of $\approx$ 10 days and peak magnitudes between (what was then considered) "typical" SLSNe and SNe (i.e., $M_{\rm peak} \sim -20$ mag). The link to rapidly evolving transients is also interesting because two objects in this category, detected and followed up in real time by iPTF and ZTF respectively, showed late-time spectra classifying them as broad-lined Type Ic SNe (iPTF16asu; Whitesides et al. 2017, and ZTF18abukavn/SN 2018gep; Ho et al. 2019). SN 2018gep is particularly interesting in this context, as its spectrum taken ~ 4 days past explosion showed features similar to the hot photospheric phase of SLSN-I, including the characteristic O II feature. At significantly higher redshift ($z = 0.677$), SN 2011kl associated with the ultra-long gamma ray burst GRB111209A also showed comparable timescales and peak luminosity to SN 2018bgv, and has been argued to show spectroscopic similarities to SLSN-I (Greiner et al. 2015; Kann et al. 2019; Liu et al. 2017b). From an empirical point of view, then, there seems to be a continuous transition between the properties of some stripped-envelope supernovae that have been considered fast, luminous transients, at least one with direct evidence of a central engine, and others that are considered SLSN-I.

The fast rise, high luminosities and blue colors of such rapidly evolving transients is often explained by either circumstellar interaction or shock cooling in an extended circumstellar medium (Drout et al. 2014; Rest et al. 2018; Whitesides et al. 2017; Ho et al. 2019). Having a naturally truncated energy input, such models can more easily explain short-duration light curves; recently Chatzopoulos & Tuminello (2019) found that CSM interaction models also did a better job of explaining SLSN-I light curves exhibiting either short-duration or symmetric light curves. However, a magnetar model, which can successfully explain both light curves and spectra of SLSN-I (Kasen & Bildsten 2010; Woosley 2010; Inserra et al. 2013; Mazzali et al. 2016; Nicholl et al. 2017b; Dessart et al. 2012; Dessart 2019), has also been considered in the context of luminous transients evolving on this timescale (Greiner et al. 2015; Whitesides et al. 2017; Wang et al. 2019). To investigate whether a magnetar model can still account for the unusual properties of SN 2018bgv, we use the code `MOSFiT` (Guillochon et al. 2018). We find that a magnetar model can reproduce the multiband light curve of SN 2018bgv with the following key parameters: ejecta mass $M_{\rm ej} = 1.35^{+0.27}_{-0.22}$ $M_\odot$, magnetic field $B = 4.80^{+2.66}_{-1.59} \times 10^{14}$ G, and initial spin $P = 7.24^{+1.28}_{-1.63}$ ms. Compared to the SLSN sample analyzed with `MOSFiT` in Nicholl et al. (2017b), this would make SN 2018bgv an outlier in all three properties: it has both a lower ejecta mass, higher magnetic field and slower initial spin than any object in their literature sample. This is not in itself an argument against SN 2018bgv being magnetar-powered, however, but rather another manifestation that the light curve properties of SN 2018bgv are unusual among SLSNe observed to date. The low ejecta

mass (and relatively high velocities) result in a short diffusion time, necessary to produce the fast rise, but the derived ejecta mass is still within the range found for SN Ic in the literature, if on the low side (e.g. Drout et al. 2011; Taddia et al. 2018; Prentice et al. 2019). Thus, we find that a fast-rising object like SN 2018bgv can still plausibly be powered by a magnetar, but requires slightly different parameters than the population of SLSNe observed to date. Finally, SN 2018bgv may be explained by a binary neutron star (like binary pulsar PSR J0737-3039A/B) model where a low mass ejecta from a new born magnetar is interacting with pulsar wind from the secondary NS companion (Hotokezaka et al. 2017).

6.1.2. *Understanding the Bumpy Light Curve of SN 2018don*

Like SN 2018bgv, SN 2018don stands out from "typical" previously observed SLSN-I in multiple ways. To begin with, our classification of this object as a SLSN-I relies on its spectroscopic similarity to SN 2007bi (Figure 4) and the corresponding assumption that the supernova is experiencing significant host galaxy extinction. Even if not reddened, however, SN 2018don would remain a highly unusual object: in this case it would be classified as an intrinsically long-lived, luminous and red SN Ic.

Going by the assumption that SN 2018don is best described as a SN 2007bi-like SLSN-I, it joins a small but growing sample of such objects showing significant light curve undulations on the decline. Such undulations have been seen in a number of objects, including SN 2007bi itself (Gal-Yam et al. 2009) and PS1-14bj (Lunnan et al. 2016), though one of the most striking examples is SN 2015bn (Nicholl et al. 2016), which had densely sampled multiband photometry and spectroscopy out to $\gtrsim 100$ days past peak light. Other examples of prominent light curve undulations in SLSN-I include PS1-12cil (Lunnan et al. 2018a), iPTF15esb (Yan et al. 2017), iPTF13dcc (Vreeswijk et al. 2017) and PS16aqv (Blanchard et al. 2018b); as was also seen in SN 2015bn and iPTF15esb, the undulations in SN 2018don are more prominent in the bluer bands.

Such light curve undulations are not easily explained by powering mechanism such as radioactive decay or magnetar spin-down, which produce smoothly decaying light curves, at least under the simplifying assumption of complete energy trapping and constant opacity. Thus, explanations for light curve bumps and undulations generally involve either changes in the opacity, or an alternative power source. For example, the model of Metzger et al. (2014) predicts a UV breakout when the O II layer reaches the ejecta surface, leading to a rapid drop in UV opacity. This explanation was considered by Nicholl et al. (2016) for the "knee" in the light curve of SN 2015bn around 30 days, which is also a similar timescale as the temporary flattening seen in SN 2018don. In SN 2015bn this change was also associated with a change in the spectrum, which transitioned from the hot photospheric phase showing O II features prior to the light curve "knee", and displayed features typical of the cool photospheric phase afterwards. Given that SN 2018don shows features typical of the cool photospheric phase also before the light curve drop and plateau, it is less clear that the same explanation will apply here, however.

Alternatively, it has been suggested that such light curve undulations result from circumstellar interaction, either in a light curve entirely powered by interaction, or as a modulation of the light curve on top of another power source such as radioactive decay or magnetar spin-down. Some SN IIn (whose narrow hydrogen lines in the spectra are a tell-tale sign of CSM interaction) have been seen to exhibit such light curve bumps (e.g. SN 2006jd; Stritzinger et al. 2012, SN 2013Z; Nyholm et al. 2017; see also

the recent compilation in Nyholm et al. 2019). In an interaction scenario, such light curve changes are naturally explained as the ejecta encounters a change in the CSM density; light curves with multiple peaks/bumps therefore require a CSM structure that deviates from a smooth profile (such as the $\rho \propto r^{-2}$ profile expected from a stellar wind). Light curves of several SLSN-I showing bumps have been successfully modelled as powered by interaction with multiple shells of circumstellar material (Liu et al. 2018). Such a CSM structure could arise from an eruptive mass-loss history; SLSNe in particular have been linked with stars encountering the pulsational pair-instability in their final stages of evolution (Woosley et al. 2007; Chatzopoulos & Wheeler 2012; Woosley 2017), leading to the ejection of multiple shells of material. Several SLSN-I, including iPTF15esb, have also shown late-time Hα emission, interpreted as arising from the supernova ejecta interacting with a H-rich CSM shell (Yan et al. 2015, 2017). Recently, a CSM shell around a SLSN was also detected directly through a resonance scattering light echo (Lunnan et al. 2018b). Thus, although SLSN-I spectra (including SN 2018don) generally do not show classical signatures of CSM interaction in the form of narrow emission lines, there is increasing evidence that some SLSN-I progenitors experience significant, eruptive mass loss prior to explosion. As such, we consider CSM interaction a plausible explanation for the light curve variations seen in SN 2018don, although a detailed exploration of the density profile required is out of the scope of this paper.

6.2. *Strategies for selecting SLSNe from large data sets*

The objects discussed in this paper, while few, serve to illustrate several challenges in identifying SLSNe in large, photometric data sets, particularly in real-time. As previous compilation studies have found that SLSNe generally exhibit slower timescales than SN Ibc and SN Ia (Nicholl et al. 2015; Lunnan et al. 2018a; De Cia et al. 2018), filtering on long observed rise times is one obvious strategy for reducing contamination from more common SNe. Such a strategy would have missed an object like SN 2018bgv, and insofar as none of the large surveys presenting samples on SLSNe to date have been spectroscopically complete, it is tricky to ascertain whether such short-timescale SLSNe are intrinsically rare or systematically missed. While SN 2018bgv, being relatively nearby for a SLSN ($z = 0.079$) and having a peak observed magnitude of ~ 17 mag probably would have been picked up for classification regardless of whether it was recognized as a likely SLSN, it is unclear whether the same had been true of a similar object at $z \sim 0.2 - 0.3$ (which was the typical redshift of SLSNe found in PTF and iPTF, De Cia et al. 2018). With correspondingly noisier photometry and slightly longer observed timescales due to time dilation, a higher-redshift analogue of SN 2018bgv would be harder to distinguish against the background of SN Ia.

However, a striking property distinguishing SN 2018bgv from SN Ia is its color, showing $g - r \simeq -0.4$ mag at peak, while SN Ia typically show $g - r \simeq 0$ mag (Miller et al. 2017). We note that the objects with the fastest rise timescales in the PS1 SLSN-I sample are also the ones with the highest measured blackbody temperatures (Lunnan et al. 2018a), suggesting blue colors may be a way to distinguish the faster-evolving SLSN-I. This is opposite of the trend described in Inserra et al. (2018a), however, who found that faster light curve timescales were weakly correlated with *redder* colors at peak. (Time scale in their work was measured by the light curve decline 30 days past peak in the 400 nm filter, though other works have found that rise- and decline timescales are tightly correlated in SLSNe; Nicholl et al. 2015;

De Cia et al. 2018.) The full SLSN sample from ZTF, providing well-sampled (1-3 day cadence) light curves in two filters, will be in a good position to explore this question.

Beyond light curve properties, other contextual information can also be used to pick out SLSNe. If a host galaxy redshift (photometric or spectroscopic) is available, this can be used to pick out intrinsically luminous transients; such a strategy has been successfully employed to find likely SLSNe at $z \gtrsim 2$ (Cooke et al. 2012; Moriya et al. 2019; Curtin et al. 2019). Studies assessing the discovery rate and detectability of SLSNe in LSST have also assumed that at least photometric redshifts will be available (Villar et al. 2018, 2019). Challenges with this strategy include that many SLSNe (including 3 out of the 4 discussed in this paper) are found in dwarf galaxies, requiring correspondingly deeper photometry for reliable photometric redshifts; conversely requiring host galaxies with well-determined redshifts could bias the sample towards objects in brighter host galaxies. Additionally, objects like SN 2018don shows that there can be SLSN-I with significant host galaxy reddening, which puts the absolute magnitude (as observed) outside of the range of typical SLSN-I. Similarly, it has also been suggested to exploit the fact that many SLSN-I are found in dwarf galaxies to use either host galaxy brightness/colors or the contrast between supernova and host galaxy brightness as a filter (e.g., McCrum et al. 2015). Again, while such a filter might have picked up the three objects in more "typical" SLSN-I host galaxies, it would have missed SN 2018don, which is neither brighter than its host galaxy nor located in a particularly faint or blue host galaxy. The diversity displayed in the first SLSNe discovered by ZTF thus illustrates that no single parameter cut is sufficient to distinguish SLSNe from other types, and we face several challenges in selecting SLSNe from a large data stream; the strategy adopted by the ZTF SLSN group will be presented in Perley et al. (2019, in preparation).

7. CONCLUSIONS

We have presented light curves and spectra of four luminous supernovae found during the first months of the ZTF survey, and argue that they can all be classified spectroscopically as SLSN-I. Of the four, only SN 2018bym resembles a "classical" SLSN-I as defined by an absolute magnitude < -21 mag (Gal-Yam 2012), or as by falling into the "4OPS" parameter space defined statistically by Inserra et al. (2018a). This variety echoes recent results from previous untargeted transient surveys, which have shown that the diversity in spectroscopically classified SLSN-I is larger than was found in the earlier literature samples (Lunnan et al. 2018a; De Cia et al. 2018; Angus et al. 2019).

All four SLSN-I discussed here have at least nightly (weather-permitting) light curve coverage in g and r from ZTF, allowing for excellent coverage of the rising phase of the light curve including color information, and enabling estimation of explosion times. We note in particular that SN 2018bgv shows a rise time (explosion to peak in the rest-frame g-band) of just 10 days, the fastest seen in a SLSN-I to date, and is starting to approach the area of timescale-luminosity parameter space occupied by so-called fast, blue, luminous transients. The properties of SN 2018bgv can still be explained by a magnetar-powered model, but requires an unusually small ejecta mass ($\simeq 1$ $M_\odot$) in order to reproduce the fast rise-time.

Like SN 2018bgv, SN 2018don pushes the boundaries of properties of observed SLSN-I to date, with an observed peak color of $g - r \simeq 0.7$ mag and a peak observed absolute magnitude of $r \simeq -19.0$ mag. Based on spectroscopic comparisons with SN 2007bi, we still classify this object as a SLSN-I, but with significant host galaxy reddening ($E(B-V)_{\rm host} \gtrsim 0.4$ mag). Under this assumption, SN 2018don

is compatible with previously observed SLSNe luminosity-wise, though at the faint and slowly-evolving end of the distribution. Its other striking property is significant light curve undulations post-peak, including a drop of 0.75 mag in g-band and 0.6 mag in r-band over a time period of $\sim$ 10 days, followed by a flattening before the light curve decline continues. These undulations are of the more extreme seen in SLSN-I, with iPTF15esb (which later showed signs of CSM interaction through emerging Hα emission; Yan et al. 2017) being the closest observed analogue. We speculate that interaction may also be at play in causing the undulations in SN 2018don.

The four objects presented here illustrate both the promise and challenges of finding SLSNe in large-scale surveys like ZTF. The demonstrated variety in both light curve timescales, observed colors, and host galaxy properties show how filtering on any one attribute is likely to miss objects that nevertheless should be considered SLSN-I. At the same time, the large area coverage and regular sampling in two filters by ZTF shows great promise in further mapping out the properties of SLSN-I, in particular increasing the sample of SLSNe with coverage through both the rise and decline and with continuous color information. As the detection efficiency during science validation will be low compared to the full survey (due to both lack of reference coverage and to algorithms still being tuned), the discovery rate of SLSNe in ZTF over the lifetime of the survey is expected to be considerably higher than these four objects over a time period of two months would suggest. Future work, including discussions on candidate selection, completeness, rates and the properties of the first SLSN-I sample from ZTF (Perley et al., in preparation; Yan et al., in preparation) will explore these questions in detail.

Based on observations obtained with the Samuel Oschin Telescope 48-inch and the 60-inch Telescope at the Palomar Observatory as part of the Zwicky Transient Facility project. ZTF is supported by the National Science Foundation under Grant No. AST-1440341 and a collaboration including Caltech, IPAC, the Weizmann Institute for Science, the Oskar Klein Center at Stockholm University, the University of Maryland, the University of Washington, Deutsches Elektronen-Synchrotron and Humboldt University, Los Alamos National Laboratories, the TANGO Consortium of Taiwan, the University of Wisconsin at Milwaukee, and Lawrence Berkeley National Laboratories. Operations are conducted by COO, IPAC, and UW. The Liverpool Telescope is operated on the island of La Palma by Liverpool John Moores University in the Spanish Observatorio del Roque de los Muchachos of the Instituto de Astrofisica de Canarias with financial support from the UK Science and Technology Facilities Council. This research has made use of data obtained through the High Energy Astrophysics Science Archive Research Center Online Service, provided by the NASA/Goddard Space Flight Center. The ZTF forced-photometry service was funded under the Heising-Simons Foundation grant #12540303 (PI: Graham). This work was supported by the GROWTH project funded by the National Science Foundation under Grant No 1545949. AGYs research is supported by the EU via ERC grant No. 725161, the ISF GW excellence center, an IMOS space infrastructure grant and the BSF Transformative program as well as The Benoziyo Endowment Fund for the Advancement of Science, the Deloro Institute for Advanced Research in Space and Optics, The Veronika A. Rabl Physics Discretionary Fund, Paul and Tina Gardner and the WIS-CIT joint research grant; AGY is the recipient of the Helen and Martin Kimmel Award for Innovative

Investigation. R.L. is supported by a Marie Skłodowska-Curie Individual Fellowship within the Horizon 2020 European Union (EU) Framework Programme for Research and Innovation (H2020-MSCA-IF-2017-794467).

Facilities: PO:1.2m, PO:Hale, Liverpool:2m, NOT, Keck:I

Software: `george` (Ambikasaran et al. 2015), `heasoft` (https://heasarc.nasa.gov/lheasoft/), `LAMBDAR` (Wright et al. 2016), `MOSFiT` (Guillochon et al. 2018), `PhotoFit` (Soumagnac et al. 2019)

REFERENCES

Ambikasaran, S., Foreman-Mackey, D., Greengard, L., Hogg, D. W., & O'Neil, M. 2015, IEEE Transactions on Pattern Analysis and Machine Intelligence, 38, arXiv:1403.6015

Angus, C. R., Levan, A. J., Perley, D. A., et al. 2016, MNRAS, 458, 84

Angus, C. R., Smith, M., Sullivan, M., et al. 2019, MNRAS, 487, 2215

Arcavi, I., Wolf, W. M., Howell, D. A., et al. 2016, ApJ, 819, 35

Barkat, Z., Rakavy, G., & Sack, N. 1967, Physical Review Letters, 18, 379

Bellm, E. C., & Sesar, B. 2016, pyraf-dbsp: Reduction pipeline for the Palomar Double Beam Spectrograph, , , ascl:1602.002

Bellm, E. C., Kulkarni, S. R., Graham, M. J., et al. 2019a, PASP, 131, 018002

Bellm, E. C., Kulkarni, S. R., Barlow, T., et al. 2019b, PASP, 131, 068003

Bhirombhakdi, K., Chornock, R., Margutti, R., et al. 2018, ApJL, 868, L32

Blanchard, P., Gomez, S., Berger, E., et al. 2018a, The Astronomer's Telegram, 11714

Blanchard, P. K., Nicholl, M., Berger, E., et al. 2018b, ApJ, 865, 9

Blanton, M. R., & Roweis, S. 2007, AJ, 133, 734

Blondin, S., & Tonry, J. L. 2007, ApJ, 666, 1024

Bose, S., Dong, S., Pastorello, A., et al. 2018, ApJ, 853, 57

Bourne, N., Maddox, S. J., Dunne, L., et al. 2012, MNRAS, 421, 3027

Branch, D., Benetti, S., Kasen, D., et al. 2002, ApJ, 566, 1005

Chambers, K. C., Magnier, E. A., Metcalfe, N., et al. 2016, arXiv e-prints, arXiv:1612.05560

Chambers, K. C., Huber, M. E., Flewelling, H., et al. 2018, Transient Name Server Discovery Report, 2018-972, 1

Chatzopoulos, E., & Tuminello, R. 2019, ApJ, 874, 68

Chatzopoulos, E., & Wheeler, J. C. 2012, ApJ, 760, 154

Chatzopoulos, E., Wheeler, J. C., & Vinko, J. 2012, ApJ, 746, 121

Chen, T.-W., Smartt, S. J., Yates, R. M., et al. 2017a, MNRAS, 470, 3566

Chen, T.-W., Schady, P., Xiao, L., et al. 2017b, ApJL, 849, L4

Chevalier, R. A., & Irwin, C. M. 2011, ApJL, 729, L6

Cooke, J., Sullivan, M., Gal-Yam, A., et al. 2012, Nature, 491, 228

Curtin, C., Cooke, J., Moriya, T. J., et al. 2019, ApJS, 241, 17

Cutri, R. M., Wright, E. L., Conrow, T., et al. 2013, Explanatory Supplement to the AllWISE Data Release Products, Tech. rep.

De Cia, A., Gal-Yam, A., Rubin, A., et al. 2018, ApJ, 860, 100

Dekany, R., Smith, R. M., Belicki, J., et al. 2016, in Society of Photo-Optical Instrumentation Engineers (SPIE) Conference Series, Vol. 9908, Ground-based and Airborne Instrumentation for Astronomy VI, 99085M

Delgado, A., Harrison, D., Hodgkin, S., et al. 2018a, Transient Name Server Discovery Report, 2018-498, 1

—. 2018b, Transient Name Server Discovery Report, 2018-599, 1

Dessart, L. 2019, A&A, 621, A141

Dessart, L., Hillier, D. J., Waldman, R., Livne, E., & Blondin, S. 2012, MNRAS, 426, L76

Dong, S., Bose, S., Siltala, L., et al. 2018, The Astronomer's Telegram, 11654

Drout, M. R., Soderberg, A. M., Gal-Yam, A., et al. 2011, ApJ, 741, 97

Drout, M. R., Chornock, R., Soderberg, A. M., et al. 2014, ApJ, 794, 23
Duev, D. A., Mahabal, A., Masci, F. J., et al. 2019, MNRAS, 2039
Eftekhari, T., Berger, E., Margalit, B., et al. 2019, ApJL, 876, L10
Flewelling, H. A., Magnier, E. A., Chambers, K. C., et al. 2016, arXiv e-prints, arXiv:1612.05243
Foreman-Mackey, D., Hogg, D. W., Lang, D., & Goodman, J. 2013, PASP, 125, 306
Fremling, C., Sharma, Y., Kulkarni, S. R., et al. 2018, The Astronomer's Telegram, 11688
Fremling, C., Sollerman, J., Taddia, F., et al. 2016, A&A, 593, A68
Gaia Collaboration, Prusti, T., de Bruijne, J. H. J., et al. 2016, A&A, 595, A1
Gal-Yam, A. 2012, Science, 337, 927
—. 2019, ARA&A, 57, 305
Gal-Yam, A., Mazzali, P., Ofek, E. O., et al. 2009, Nature, 462, 624
Gehrels, N., Chincarini, G., Giommi, P., et al. 2004, ApJ, 611, 1005
Gezari, S., Halpern, J. P., Grupe, D., et al. 2009, ApJ, 690, 1313
Gomez, S., Berger, E., Nicholl, M., et al. 2019, ApJ, 881, 87
Graham, M. J., Kulkarni, S. R., Bellm, E. C., et al. 2019, PASP, 131, 078001
Greiner, J., Mazzali, P. A., Kann, D. A., et al. 2015, Nature, 523, 189
Guillochon, J., Nicholl, M., Villar, V. A., et al. 2018, ApJS, 236, 6
Guillochon, J., Parrent, J., Kelley, L. Z., & Margutti, R. 2017, ApJ, 835, 64
Heger, A., & Woosley, S. E. 2002, ApJ, 567, 532
Ho, A. Y. Q., Goldstein, D. A., Schulze, S., et al. 2019, arXiv e-prints, arXiv:1904.11009
Hotokezaka, K., Kashiyama, K., & Murase, K. 2017, The Astrophysical Journal, 850, 18
Howell, D. A., Sullivan, M., Perrett, K., et al. 2005, ApJ, 634, 1190
Inserra, C., Prajs, S., Gutierrez, C. P., et al. 2018a, ApJ, 854, 175
Inserra, C., Smartt, S. J., Jerkstrand, A., et al. 2013, ApJ, 770, 128
Inserra, C., Smartt, S. J., Gall, E. E. E., et al. 2018b, MNRAS, 475, 1046
Izzo, L., Thöne, C. C., García-Benito, R., et al. 2018, A&A, 610, A11
Jerkstrand, A., Smartt, S. J., & Heger, A. 2016, MNRAS, 455, 3207
Kann, D. A., Schady, P., Olivares E., F., et al. 2019, A&A, 624, A143
Kasen, D., & Bildsten, L. 2010, ApJ, 717, 245
Kasliwal, M. M., Cannella, C., Bagdasaryan, A., et al. 2019, PASP, 131, 038003
Komatsu, E., Smith, K. M., Dunkley, J., et al. 2011, ApJs, 192, 18
Kriek, M., van Dokkum, P. G., Labbé, I., et al. 2009, ApJ, 700, 221
Kulkarni, S. R., Perley, D. A., & Miller, A. A. 2018, ApJ, 860, 22
Lang, D. 2014, AJ, 147, 108
Leloudas, G., Schulze, S., Krühler, T., et al. 2015, MNRAS, 449, 917
Liu, L.-D., Wang, L.-J., Wang, S.-Q., & Dai, Z.-G. 2018, ApJ, 856, 59
Liu, L.-D., Wang, S.-Q., Wang, L.-J., et al. 2017a, ApJ, 842, 26
Liu, Y.-Q., Modjaz, M., & Bianco, F. B. 2017b, ApJ, 845, 85
Lunnan, R., Chornock, R., Berger, E., et al. 2013, ApJ, 771, 97
—. 2014, ApJ, 787, 138
—. 2015, ApJ, 804, 90
—. 2016, ApJ, 831, 144
—. 2018a, ApJ, 852, 81
Lunnan, R., Fransson, C., Vreeswijk, P. M., et al. 2018b, Nature Astronomy, 2, 887
Mahabal, A., Rebbapragada, U., Walters, R., et al. 2019, PASP, 131, 038002
Maraston, C. 2005, MNRAS, 362, 799
Margutti, R., Chornock, R., Metzger, B. D., et al. 2018, ApJ, 864, 45
Martin, D. C., Fanson, J., Schiminovich, D., et al. 2005, ApJL, 619, L1
Masci, F. J., Laher, R. R., Rusholme, B., et al. 2019, PASP, 131, 018003
Mazzali, P. A., Sullivan, M., Pian, E., Greiner, J., & Kann, D. A. 2016, MNRAS, 458, 3455
McCrum, M., Smartt, S. J., Rest, A., et al. 2015, MNRAS, 448, 1206
Meisner, A. M., Lang, D., & Schlegel, D. J. 2017, AJ, 153, 38
Metzger, B. D., Vurm, I., Hascoët, R., & Beloborodov, A. M. 2014, MNRAS, 437, 703
Miller, A. A., Chornock, R., Perley, D. A., et al. 2009, ApJ, 690, 1303

Miller, A. A., Kasliwal, M. M., Cao, Y., et al. 2017, The Astrophysical Journal, 848, 59
Modjaz, M., Liu, Y. Q., Bianco, F. B., & Graur, O. 2016, ApJ, 832, 108
Moriya, T. J., Blinnikov, S. I., Tominaga, N., et al. 2013, MNRAS, 428, 1020
Moriya, T. J., Tanaka, M., Yasuda, N., et al. 2019, ApJS, 241, 16
Morrissey, P., Conrow, T., Barlow, T. A., et al. 2007, ApJS, 173, 682
Nicholl, M., Berger, E., Margutti, R., et al. 2017a, ApJL, 845, L8
Nicholl, M., Gomez, S., Blanchard, P., & Berger, E. 2018a, The Astronomer's Telegram, 11648
Nicholl, M., Guillochon, J., & Berger, E. 2017b, ApJ, 850, 55
Nicholl, M., & Smartt, S. J. 2016, MNRAS, 457, L79
Nicholl, M., Smartt, S. J., Jerkstrand, A., et al. 2013, Nature, 502, 346
—. 2015, MNRAS, 452, 3869
Nicholl, M., Berger, E., Smartt, S. J., et al. 2016, ApJ, 826, 39
Nicholl, M., Blanchard, P. K., Berger, E., et al. 2018b, ApJL, 866, L24
Nyholm, A., Sollerman, J., Taddia, F., et al. 2017, A&A, 605, A6
Nyholm, A., Sollerman, J., Tartaglia, L., et al. 2019, arXiv e-prints, arXiv:1906.05812
Ofek, E. O. 2014, MATLAB package for astronomy and astrophysics, Astrophysics Source Code Library, , , ascl:1407.005
Oke, J. B., & Gunn, J. E. 1982, PASP, 94, 586
Oke, J. B., Cohen, J. G., Carr, M., et al. 1995, PASP, 107, 375
Pastorello, A., Smartt, S. J., Botticella, M. T., et al. 2010, ApJL, 724, L16
Patterson, M. T., Bellm, E. C., Rusholme, B., et al. 2019, PASP, 131, 018001
Perley, D. A. 2019, PASP, 131, 084503
Perley, D. A., Quimby, R. M., Yan, L., et al. 2016, ApJ, 830, 13
Piascik, A. S., Steele, I. A., Bates, S. D., et al. 2014, in Society of Photo-Optical Instrumentation Engineers (SPIE) Conference Series, Vol. 9147, Ground-based and Airborne Instrumentation for Astronomy V, 91478H
Prentice, S. J., Ashall, C., James, P. A., et al. 2019, MNRAS, 485, 1559
Pursiainen, M., Childress, M., Smith, M., et al. 2018, MNRAS, 481, 894
Quimby, R. M., Kulkarni, S. R., Kasliwal, M. M., et al. 2011, Nature, 474, 487
Quimby, R. M., De Cia, A., Gal-Yam, A., et al. 2018, ApJ, 855, 2
Rau, A., Kulkarni, S. R., Law, N. M., et al. 2009, PASP, 121, 1334
Rest, A., Garnavich, P. M., Khatami, D., et al. 2018, Nature Astronomy, 2, 307
Roming, P. W. A., Kennedy, T. E., Mason, K. O., et al. 2005, SSRv, 120, 95
Schlafly, E. F., & Finkbeiner, D. P. 2011, ApJ, 737, 103
Schulze, S., Krühler, T., Leloudas, G., et al. 2018, MNRAS, 473, 1258
Shappee, B. J., Prieto, J. L., Grupe, D., et al. 2014, ApJ, 788, 48
Skrutskie, M. F., Cutri, R. M., Stiening, R., et al. 2006, AJ, 131, 1163
Sorokina, E., Blinnikov, S., Nomoto, K., Quimby, R., & Tolstov, A. 2016, ApJ, 829, 17
Soumagnac, M. T., Ganot, N., Gal-yam, A., et al. 2019, arXiv e-prints, arXiv:1907.11252
Steele, I. A., Smith, R. J., Rees, P. C., et al. 2004, in Proc. SPIE, Vol. 5489, Ground-based Telescopes, ed. J. M. Oschmann, Jr., 679–692
Stritzinger, M., Taddia, F., Fransson, C., et al. 2012, ApJ, 756, 173
Tachibana, Y., & Miller, A. A. 2018, Publications of the Astronomical Society of the Pacific, 130, 128001
Taddia, F., Stritzinger, M. D., Bersten, M., et al. 2018, A&A, 609, A136
Tonry, J., Stalder, B., Denneau, L., et al. 2018a, Transient Name Server Discovery Report, 2018-707, 1
Tonry, J. L., Denneau, L., Heinze, A. N., et al. 2018b, PASP, 130, 064505
Villar, V. A., Nicholl, M., & Berger, E. 2018, ApJ, 869, 166
Villar, V. A., Berger, E., Miller, G., et al. 2019, arXiv e-prints, arXiv:1905.07422
Vreeswijk, P. M., Leloudas, G., Gal-Yam, A., et al. 2017, ApJ, 835, 58
Wang, S.-Q., Wang, L.-J., Li, L., et al. 2019, arXiv e-prints, arXiv:1904.09604
Wheeler, J. C., Chatzopoulos, E., Vinkó, J., & Tuminello, R. 2017, ApJL, 851, L14

Whitesides, L., Lunnan, R., Kasliwal, M. M., et al. 2017, ApJ, 851, 107

Woosley, S. E. 2010, ApJL, 719, L204

—. 2017, ApJ, 836, 244

Woosley, S. E., Blinnikov, S., & Heger, A. 2007, Nature, 450, 390

Wright, A. H., Robotham, A. S. G., Bourne, N., et al. 2016, MNRAS, 460, 765

Yan, L., Perley, D. A., De Cia, A., et al. 2018, The Astrophysical Journal, 858, 91

Yan, L., Quimby, R., Ofek, E., et al. 2015, ApJ, 814, 108

Yan, L., Lunnan, R., Perley, D. A., et al. 2017, ApJ, 848, 6

York, D. G., Adelman, J., Anderson, John E., J., et al. 2000, AJ, 120, 1579

Zackay, B., Ofek, E. O., & Gal-Yam, A. 2016, ApJ, 830, 27

Table 1. List of SLSNe

ZTF name	IAU name	RA (J2000)	Dec (J2000)	Redshift	E(B-V)[a] (mag)
ZTF18aaisyyp	SN 2018avk	$13^h11^m27.72^s$	$+65°38'16.7''$	0.132	0.012
ZTF18aapgrxo	SN 2018bym	$18^h43^m13.42^s$	$+45°12'28.2''$	0.274	0.052
ZTF18aavrmcg	SN 2018bgv	$11^h02^m30.29^s$	$+55°35'55.8''$	0.079	0.008
ZTF18aajqcue	SN 2018don	$13^h55^m08.65^s$	$+58°29'42.0''$	0.073	0.009

[a]From Schlafly & Finkbeiner (2011)

Table 2. Photometry

Object	MJD (days)	Phase (rest-frame days)	Filter	AB mag	Telescope+Instrument
SN 2018bym	58232.5	-37.7	g	20.82 ± 0.13	P48+ZTF
SN 2018bym	58232.5	-37.7	g	20.52 ± 0.11	P48+ZTF
SN 2018bym	58234.4	-36.2	g	> 20.30	P48+ZTF
SN 2018bym	58234.4	-36.2	g	> 20.30	P48+ZTF
SN 2018bym	58234.5	-36.2	g	20.43 ± 0.14	P48+ZTF
SN 2018bym	58234.5	-36.2	g	20.61 ± 0.18	P48+ZTF
SN 2018bym	58234.5	-36.1	g	20.60 ± 0.18	P48+ZTF
SN 2018bym	58235.4	-35.4	g	20.42 ± 0.25	P48+ZTF
SN 2018bym	58235.4	-35.4	g	20.19 ± 0.20	P48+ZTF
SN 2018bym	58235.4	-35.4	g	20.17 ± 0.22	P48+ZTF

Note—The full table is available in electronic form. A portion is shown here for guidance.

Table 3. Summary of Spectroscopic Observations

Object	Observation Date (YYYY MM DD.D)	Phase (rest-frame days)	Telescope+Instrument	Grating[a]	Exp. time[a] (s)	Airmass
SN 2018avk	2018 May 04	-11.66	NOT+ALFOSC	Gr 4	1800	1.3
SN 2018avk	2018 May 14.3	-2.56	KeckI+LRIS	400/3400,400/8500	840,800	1.4
SN 2018bym	2018 May 31	-9.34	NOT+ALFOSC	Gr 4	2400	1.4
SN 2018bym	2018 Jun 12	+0.08	P200+DBSP	600/4000,316/7500	600	1.13
SN 2018bym	2018 Jun 17.5	+4.4	KeckI+LRIS	400/3400,400/8500	600,570	1.4
SN 2018bym	2018 Jul 12.6	+24.10	KeckI+LRIS	400/3400,400/8500	600,600	2.0
SN 2018bgv	2018 May 20	+4.45	LT+SPRAT	Wasatch600	300	1.6
SN 2018bgv	2018 May 23	+7.23	NOT+ALFOSC	Gr 4	2×2400	1.3
SN 2018bgv	2018 May 31	+14.64	NOT+ALFOSC	Gr 4	900	1.3
SN 2018bgv	2018 Jun 04	+18.34	NOT+ALFOSC	Gr 4	2x2400	1.4
SN 2018bgv	2018 Jun 10	+23.90	NOT+ALFOSC	Gr 4	900	1.3
SN 2018bgv	2018 Jun 13	+26.68	NOT+ALFOSC	Gr 4	2×2400	1.3
SN 2018bgv	2018 Jul 17	+58.18	P200+DBSP	600/4000,316/7500	1200	1.7
SN 2018don	2018 May 16.3	-12.95	P200+DBSP	600/4000,316/7500	900	1.2
SN 2018don	2018 May 16.9	-12.39	LT+SPRAT	Wasatch600	300	1.2
SN 2018don	2018 May 30	-0.19	NOT+ALFOSC	Gr 4	2×2400	1.1
SN 2018don	2018 Jun 09.4	+9.50	P200+DBSP	600/4000,316/7500	900	1.6
SN 2018don	2018 Jun 25	+24.04	NOT+ALFOSC	Gr 4	2×2400	1.2
SN 2018don	2018 Jul 17.2	+44.72	P200+DBSP	600/4000,316/7500	600	1.4

[a] Comma-separated values indicate setup for blue and red arms, respectively.

Table 4. Host Galaxy Photometry

Object	Filter	AB mag	Telescope
SN 2018avk	g	23.26 ± 0.12	SDSS
SN 2018avk	r	22.45 ± 0.12	SDSS
SN 2018avk	i	22.44 ± 0.16	SDSS
SN 2018avk	$g_{\rm P1}$	23.26 ± 0.22	PS1
SN 2018avk	$r_{\rm P1}$	22.51 ± 0.12	PS1
SN 2018avk	$i_{\rm P1}$	22.88 ± 0.12	PS1
SN 2018bym	g	23.02 ± 0.16	CFHT
SN 2018bym	r	22.42 ± 0.06	CFHT
SN 2018bym	$r_{\rm P1}$	22.46 ± 0.19	PS1
SN 2018bym	$i_{\rm P1}$	22.35 ± 0.14	PS1
SN 2018don	NUV	22.01 ± 0.14	GALEX
SN 2018don	u	20.37 ± 0.17	SDSS
SN 2018don	g	18.99 ± 0.03	SDSS
SN 2018don	r	18.26 ± 0.02	SDSS
SN 2018don	i	17.92 ± 0.02	SDSS
SN 2018don	z	17.60 ± 0.07	SDSS
SN 2018don	$g_{\rm P1}$	19.04 ± 0.04	PS1
SN 2018don	$r_{\rm P1}$	18.31 ± 0.02	PS1
SN 2018don	$i_{\rm P1}$	17.98 ± 0.04	PS1
SN 2018don	$z_{\rm P1}$	17.77 ± 0.04	PS1
SN 2018don	$y_{\rm P1}$	17.58 ± 0.09	PS1
SN 2018don	J	17.23 ± 0.18	2MASS
SN 2018don	H	17.38 ± 0.32	2MASS
SN 2018don	K	17.46 ± 0.28	2MASS
SN 2018don	$W1$	17.94 ± 0.05	WISE
SN 2018don	$W2$	18.28 ± 0.09	WISE
SN 2018bgv	UVW2	20.92 ± 0.07	UVOT
SN 2018bgv	UVM2	20.77 ± 0.06	UVOT
SN 2018bgv	UVW1	20.60 ± 0.12	UVOT
SN 2018bgv	U	20.72 ± 0.26	UVOT
SN 2018bgv	u	20.96 ± 0.14	SDSS
SN 2018bgv	g	19.96 ± 0.03	SDSS
SN 2018bgv	r	19.74 ± 0.07	SDSS
SN 2018bgv	i	19.26 ± 0.06	SDSS
SN 2018bgv	z	19.23 ± 0.16	SDSS
SN 2018bgv	$g_{\rm P1}$	19.93 ± 0.03	PS1
SN 2018bgv	$r_{\rm P1}$	19.70 ± 0.06	PS1
SN 2018bgv	$i_{\rm P1}$	19.44 ± 0.06	PS1
SN 2018bgv	$z_{\rm P1}$	19.42 ± 0.09	PS1
SN 2018bgv	$y_{\rm P1}$	19.61 ± 0.14	PS1
SN 2018bgv	J	19.26 ± 0.32	2MASS
SN 2018bgv	$W1$	20.12 ± 0.11	WISE

Table 5. Summary of Light Curve Properties

Object	g-band Peak Date (MJD)	g-band Peak Luminosity (mag)	Explosion date[a] (MJD)	g-band rise ($t_{1/2}$) (rest-frame days)	g-band decline ($t_{1/2}$) (rest-frame days)
SN 2018avk	58255.2	−20.30	58199.0 ± 0.3	35	67
SN 2018bym	58280.9	−22.05	58230.1 ± 0.5	24	30
SN 2018bgv	58253.2	−20.68	58242.5 ± 0.1	7	17
SN 2018don	58268.2	−18.65[b]	58213.6 ± 0.5	33	36

[a] Assuming the rise in flux is described by a second-order polynomial. Quoted error bars include statistical uncertainty only, and do not account for e.g. systematic uncertainty comparing different functional forms for the rise.

[b] If assuming E(B-V) = 0.4 mag, the reddening-corrected g-band peak magnitude would be −20.09 mag.

Table 6. Summary of Host Galaxy Properties

Object	$\log_{10}$(Stellar Mass) ($M_\odot$)	A_V (mag)	$\log_{10}$(Age) (yr)	SFR ($M_\odot$ $yr^{-}1$)
SN 2018avk	$7.82^{+0.07}_{-0.08}$	$0.03^{+0.00}_{-0.03}$	$8.40^{+0.51}_{-0.15}$	···
SN 2018don	$9.78^{+0.16}_{-0.28}$	$0.00^{+1.81}_{-0.00}$	$9.50^{+0.29}_{-1.35}$	$0.087^{+6.222}_{-0.008}$
SN 2018bym	$8.58^{+0.38}_{-0.64}$	$0.03^{+1.41}_{-0.03}$	$8.20^{+1.22}_{-1.38}$	···
SN 2018bgv	$8.64^{+0.11}_{-0.10}$	$0.00^{+0.14}_{-0.00}$	$9.00^{+0.31}_{-0.33}$	$0.316^{+0.120}_{-0.047}$